Journal of Materials Processing Tech. 348 (2026) 119183

Contents lists available at ScienceDirect

Journal of Materials Processing Tech.

journal homepage: www.elsevier.com/locate/jmatprotec

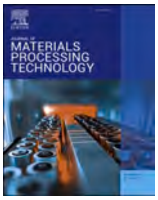

Research article

Uniform aluminum droplet deposition manufacturing in an open environment: Oxidation suppression and stable printing under coaxial shielding gas

Yi Zhou [a], Jun Luo [a,b], Lin Su [a], Lehua Qi [a,b,*]

[a] School of Mechanical Engineering, Northwestern Polytechnical University, Xi'an 710072, China
[b] Research and Development Institute of Northwestern Polytechnical University in Shenzhen, Shenzhen 518057, China

ARTICLE INFO

Keywords:
Coaxial shielding gas
Surface oxidation
Deposition dynamics
Aluminum droplet
Metal micro-droplet deposition manufacturing

ABSTRACT

Employing opening shielding gas in metal micro-droplet deposition enables lightweight, real-time, eco-friendly manufacturing. However, aluminum alloys, highly sought-after for manufacturing, face challenges in equipment development and experimental research due to their high oxidation reactivity and thermal sensitivity. This study presents a novel approach that combines piezoelectric actuation with dynamic coaxial gas shielding. The method enables stable aluminum droplet printing with micron-level precision in an open environment. Through combined experiments and theoretical models, the impact of oxidation on droplet deposition dynamics, surface morphology, and formation quality was investigated. Results show that even a slight change in the deposition distance would cause significant variations in deposition and oxidation behavior. Increasing the deposition distance not only exacerbates droplet oxidation and dampens droplet oscillation, but also forms oxidation wrinkles on the droplet surface. A higher substrate feed speed also reduces the shielding gas effectiveness. This effect is particularly significant in multi-layer droplet pileup, where heat accumulation delays solidification and exacerbates oxidation in the upper-layer droplets. To address these challenges, a variable-speed printing strategy based on thermal management was proposed. This method suppresses droplet surface oxidation, enabling metallurgical bonding and stable part formation in open environments. This work provides both practical strategies and theoretical insights for oxidation control in high-temperature metal droplet printing under open-environment conditions.

1. Introduction

Driven by the increasing demand for lightweight, instantaneous, and environment-friendly manufacturing solutions [1–3], efforts are being made to optimize 3D printing equipment, minimize machine sizes, and create portable printing platforms [4]. Among the numerous existing metal 3D printing technologies, metal micro-droplet deposition manufacturing [5,6] is particularly notable. It requires no special raw material preparation or storage, consumes relatively low energy during printing, and enables multi-material interactive printing [7–9]. This technology has been extensively utilized in fields like metal part prototyping [10,11], electronic packaging [12,13], circuit printing [14–16], and in-situ structural repair [17]. To meet the growing demand for lightweight and industrialized manufacturing, several open-environment printing approaches have been developed. These typically employ inert airflow near the nozzle to establish a localized low-oxygen atmosphere, thereby improving operational flexibility and production efficiency [18]. Considerable progress has been made in open-environment printing for tin alloy droplets. However, the extension to molten aluminum alloys remains highly challenging. The difficulty arises from the rapid oxide film formation, higher processing temperatures, chemically stable oxide layers, and stronger reactivity [19]. Given aluminum's widespread application in structural components, there is an urgent need for effective open-environment printing strategies tailored to aluminum droplets.

Although some progress has been reported, the micro-droplet deposition manufacturing for aluminum alloys remains mostly experimental. Currently, only one commercial system exists: the ElemX, developed by ADDiTEC (Additive Technologies LLC, USA), based on their proprietary 'MagnetoJet' technology [20–23]. Research on

---

* Corresponding author at: School of Mechanical Engineering, Northwestern Polytechnical University, Xi'an 710072, China.
E-mail addresses: yizhou@mail.nwpu.edu.cn (Y. Zhou), qilehua@nwpu.edu.cn (L. Qi).

https://doi.org/10.1016/j.jmatprotec.2025.119183
Received 29 July 2025; Received in revised form 9 December 2025; Accepted 10 December 2025

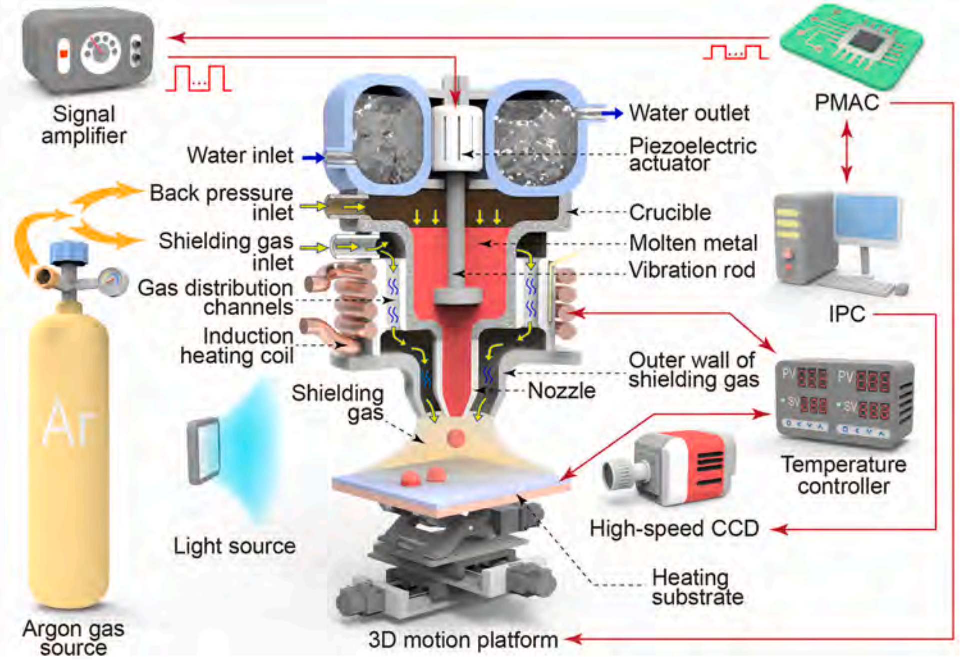

Fig. 1. Schematic diagram of the aluminum droplet open-printing system.

aluminum alloy printing under open environmental conditions is still limited. Most studies focus on tin alloys because of their lower processing temperatures and easier handling. Although tin-based methods cannot be directly applied to aluminum droplets due to significant differences in material properties, they provide useful insights. For instance, Fang et al. [24] and Amirzadeh et al. [25] employed lateral-blowing shielding gas near the nozzle to protect tin droplets, but this caused droplet trajectory deviations due to misaligned gas-droplet flow directions. To mitigate this issue, Yokoyama et al. [26,27] optimized the lateral-blowing configuration, significantly reducing airflow-induced disturbances. Tropmann et al. [28,29] proposed a StarJet technique, which involves machining star-shaped gas grooves around a standard round-hole silicon nozzle using deep reactive ion etching. This design directs inert gas precisely to the droplet ejection point, effectively enveloping the molten tin jet and enhancing shielding performance. Zhou et al. [30,31] achieved high-quality tin droplet printing using a coaxial annular gas shielding system. For aluminum droplets, the ejection system requires stricter operating temperature and low-oxygen shielding capabilities. Among the limited academic studies on open-environment aluminum droplet printing, the work by Gerdes et al. [32] provides an early demonstration of the feasibility of this process. Building on the StarJet design by Tropmann et al., they demonstrated aluminum droplet open-environment printing employing a SiC nozzle. However, their pneumatically actuated droplet generation system was highly sensitive to pressure fluctuations, which compromised printing precision and droplet consistency. The commercial ElemX system has also demonstrated aluminum alloy droplet printing under inert gas shielding [20,21]. While it achieves high frequency and industrial performance, its shielding gas delivery design and oxidation control strategies have not been detailed in peer-reviewed publications. According to some brief introductions in relevant literature [33], the shielding gas in the ElemX system flows from the nozzle's lower side to the front side before reaching the printed part. As described in the available patent [34], this configuration is similar to the lateral shielding gas supply strategy. Beyond those, reports on open-environment aluminum droplet printing remain scarce. The corrosive nature of molten aluminum limits equipment material selection and complicates shielding system design. More critically, the primary technical challenge lies in establishing a high-quality shielding gas environment. According to high-temperature oxidation kinetics for metals, the oxide film growth rate constant for aluminum alloys is 3–6 orders of magnitude higher than that for tin alloys [35,36]. This makes oxidation control far more demanding.

To mitigate the impact of oxidation during fabrication, researchers have investigated the effects of surface oxide layers on molten aluminum. K. Patouillet et al. [37–39] examined the mechanical behavior of oxide films on molten aluminum, showing that they exhibit high viscosity and shear-thinning characteristics. Shen et al. [40] demonstrated that oxidation adversely affects the wettability of molten aluminum, with thicker oxide layers leading to poorer wettability. Yang et al. [41] investigated aluminum droplet deposition under controlled oxygen levels, elucidating the effects of oxide layers on droplet spreading and recoil dynamics. These studies provide valuable theoretical insights into oxidation behavior, but are insufficient for achieving high-quality aluminum droplet printing under shielding gas. The aluminum droplet printing is governed by a complex interplay of oxidation, fluid dynamics, and thermodynamics. Yet, comprehensive studies on aluminum droplet oxidation mechanisms and control strategies in open environments are still lacking. This gap continues to hinder the advancement of aluminum droplet printing technologies and related equipment development.

To this end, this study focuses on the open-environment printing of aluminum droplets, aiming to provide both equipment solutions and theoretical insights for oxidation control and high-quality printing. High-speed imaging was utilized to capture droplet deposition dynamics. By observing the surface oxidation morphology of aluminum droplets, the oxidation mechanism on the droplet's ejection behavior, deposition dynamics, and formation quality was analyzed. Ultimately, a parameter control strategy was proposed to suppress aluminum droplet oxidation, ensure metallurgical bonding, and achieve stable structure formation under shielding gas. This work provides essential technical guidance for advancing open-environment printing of high-melting-point metals, supporting future lightweight and scalable manufacturing applications.

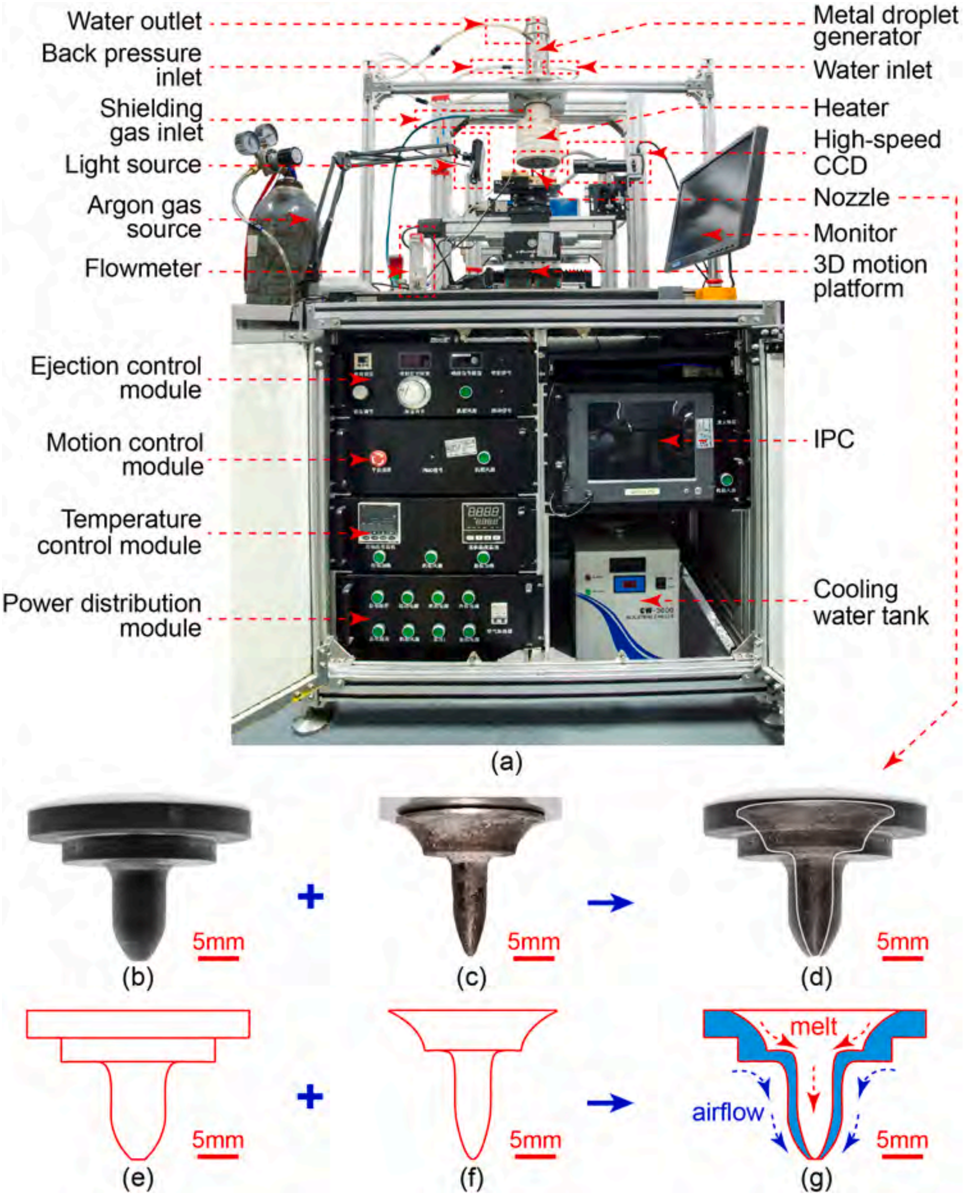

Fig. 2. (a) Developed aluminum droplet open-printing equipment. Nozzle morphology for (b) external, (c) internal, and (d) overlapped view. Nozzle contour for (e) external, (f) internal, and (g) cross-sectional.

2. Experimental methods

2.1. Printing setup and procedure

In the metal droplet ejection process, droplets are typically a few hundred micrometers in size and ejected at relatively low velocities (below 3 m/s). Among various shielding gas configurations, the coaxial annular shielding gas design has been proven both practical and reliable. By aligning the shielding gas flow with the droplet's falling direction, this configuration minimizes lateral airflow disturbances. It also maintains the droplet's flight stability and extends the effective low-oxygen protective distance. Accordingly, the aluminum droplet open-printing system developed in this study adopted a coaxial annular shielding gas setup. To ensure stable droplet generation, a piezoelectric actuation method was employed. Fig. 1 illustrates the schematic of the printing system, which consists of five main subsystems: a temperature control subsystem, a molten aluminum droplet generation subsystem, a cooling water supply subsystem, a motion control subsystem, and a coaxial shielding gas supply subsystem.

The temperature control subsystem comprises a temperature controller (Shimax Co., Ltd., Japan), a crucible, and a heating substrate, responsible for maintaining the working temperatures of both the crucible and substrate. Given that the operating temperature of the aluminum alloy exceeds 973 K, induction heating was utilized for the crucible, providing high heating efficiency with a power output exceeding 3000 W. Unlike conventional resistive heating methods, induction heating directly heats the graphite crucible via electromagnetic induction, significantly improving heating efficiency. As a result, the high-temperature exposure duration of the ejection components is greatly reduced, thereby minimizing the risk of oxidation for the components. Moreover, the induction heating can provide a more uniform and stable heating environment for the aluminum droplet ejection process. By adjusting the current frequency and power, it effectively suppresses temperature fluctuations during aluminum printing.

The molten aluminum droplet generation subsystem facilitates on-demand droplet ejection. It includes an industrial personal computer (IPC), a Programmable Multi-Axis Controller (PMAC) (Delta Tau Data Systems Inc., United States), a signal amplifier (CoreMorrow Co., Ltd.,

Table 1
The chemical composition of AlMg1SiCu aluminum alloy (wt%) [44].

Mg	Si	Cu	Cr	Fe	Zn	Mn	Ti	Al
0.8–1.2	0.4–0.8	0.15–0.4	0.04–0.35	≤ 0.7	≤ 0.25	≤ 0.15	≤ 0.15	Bal.

China), a piezoelectric ceramic (CoreMorrow Co., Ltd., China), a vibration rod, and a nozzle. After metal blocks melts in the crucible, the IPC instructs the PMAC to generate a pulse signal. The signal is amplified 12.5 times by the signal amplifier and applied to the piezoelectric ceramic. which converts the electrical signal into mechanical vibrations. The mechanical energy induces a slight perturbation in the molten metal via the vibration rod, resulting in droplet formation at the nozzle outlet. To prevent thermal degradation of the piezoelectric ceramic above its Curie point, the vibration rod is extended to reduce heat transfer. Meanwhile, circulating water is supplied around the piezoelectric ceramics for effective cooling.

The motion control subsystem consists of the PMAC, motor drivers, a 3D motion platform, and the substrate. During droplet printing, the PMAC controls the motion platform to move vertically and horizontally. This enables precise positioning for droplet deposition.

To suppress oxidation during droplet flight and deposition, the coaxial shielding gas supply subsystem delivers controlled flow of inert gas. Argon was selected for its inertness (properties listed in Table 2). The gas is supplied from a high-pressure cylinder and divided into two paths. One is directed to a back-pressure inlet for removing molten metal waste. The other is directed to a shielding gas inlet, then guided through gas channels to the nozzle outlet. To minimize gas dispersion near the nozzle, a tapered outer shielding wall surrounds the nozzle, ensuring effective gas coverage.

Molten aluminum is highly reductive and chemically aggressive, rapidly dissolving or forming brittle intermetallic compounds with most materials. This characteristic severely restricts the selection of materials for components in direct contact with molten aluminum. Graphite, however, exhibits excellent chemical stability in molten aluminum and offers high thermal and electrical conductivity [42]. Therefore, key components such as the crucible, vibration rod, nozzle, and other parts that are directly exposed to molten aluminum were fabricated from graphite. To ensure thermal insulation and electrical isolation, components in direct contact with the induction heating coil were made from mica board or asbestos board. The assembled equipment is shown in Fig. 2a.

To ensure the directional stability and laminar uniformity of the shielding gas in the coaxial annular flow system, the nozzle channel must be designed with a sufficient length-to-diameter ratio. If the flow channel is too short, the gas cannot fully develop into a stable laminar flow before exiting the nozzle. This leads to non-uniform velocity profiles, vortex formation, and undesirable droplet trajectory disturbances. Based on empirical correlations of Durst et al. [43] for laminar entrance length in annular runner, the required flow development length (L_{dev}) can be estimated as follows:

$$L_{\mathrm{dev}} = \left[(0.619)^{1.6} + (0.0567Re_{\mathrm{g}})^{1.6}\right]^{1/1.6} D_{\mathrm{h}}, \tag{1}$$

where Re_{g} is the Reynolds number of the shielding gas and D_{h} is the hydraulic diameter of the annular shielding gas channel. For the present design, the annular runner has an inner diameter of 5 mm and an outer diameter of 6 mm, resulting in $D_{\mathrm{h}} = 1.0$ mm. The corresponding Reynolds number for annular shielding gas is approximately 295, yielding a required entrance length of $L_{\mathrm{dev}} \approx 16.8$ mm. Given that the inner diameter of the nozzle is 3.5 mm, the corresponding aspect ratio for nozzle channel is 4.8. Therefore, the coaxial annular shielding gas system requires a nozzle channel with an aspect ratio greater than 5 in this work. The graphite nozzle was designed with streamlined transitions on both its interior and exterior surfaces. This minimizes turbulence in the airflow and molten metal caused by abrupt diameter changes. Fig. 2b displays the external appearance of the machined graphite nozzle. After filling the nozzle with molten aluminum, allowing it to solidify, and then demolding, the internal morphology of the nozzle was exposed, as shown in Fig. 2c. An overlapping view of the nozzle's internal and external profiles is presented in Fig. 2d. By extracting contours from the morphological images, the external, internal, and cross-sectional profiles of the nozzle were obtained, as illustrated in Fig. 2e-g, respectively. These results confirm that the machined graphite nozzle achieves a smooth, streamlined geometry while meeting the required aspect ratio.

Table 2
Properties of materials used in the experiment [45–47].

Properties	**AlMg1SiCu (Liquid at 1023 K)**	**AlMg1SiCu (Solid at 573 K)**	**Argon (Gas at 350 K)**
Density ($\mathrm{kg \cdot m^{-3}}$)	$\rho_{\mathrm{L}} = 2490$	$\rho_{\mathrm{S}} = 2705$	$\rho_{\mathrm{g}} = 1.6228$
Dynamics viscosity (Pa·s)	$\mu_{\mathrm{m}} = 1.15 \times 10^{-3}$	-	$\mu_{\mathrm{g}} = 2.125 \times 10^{-5}$
Specific heat ($\mathrm{J \cdot kg^{-1} \cdot K^{-1}}$)	$C_{\mathrm{L}} = 1050$	$C_{\mathrm{S}} = 921$	$C_{\mathrm{g}} = 521$
Thermal conductivity ($\mathrm{W \cdot m^{-1} \cdot K^{-1}}$)	$k_{\mathrm{L}} = 90$	$k_{\mathrm{S}} = 195$	$k_{\mathrm{g}} = 0.017$
Liquidus temperature (K)	$T_{\mathrm{L}} = 915.15$	-	-
Solidus temperature (K)	-	$T_{\mathrm{S}} = 873.15$	-
Latent heat of fusion (J/kg)	-	$H_{\mathrm{f}} = 3.97 \times 10^{5}$	-
Surface tension ($\mathrm{N \cdot m^{-1}}$)	$\sigma = 0.871$	-	-

2.2. *Experimental materials and preparation*

AlMg1SiCu was selected as both the printing and substrate material. Its chemical composition [44] and physical properties [45–47] are listed in Tables 1 and 2, respectively. Prior to the experiment, the oxide layer on the aluminum alloy surface was mechanically removed. To prevent re-oxidation during heating, argon gas was supplied before starting the induction heater. Inert gas was continuously delivered to both the backpressure and shielding gas inlets at 3 L/min for 15 min to purge residual air from the system. After purging, the backpressure gas was shut off. The shielding gas supply rate was then reduced to 1.5 L/min to prevent air backflow into the nozzle.

2.3. *Characterization methods*

The ejection and deposition processes of aluminum droplets were recorded using an iX-Speed 220 CCD camera (iX Cameras Ltd., United Kingdom) at 10,000 fps with a resolution of 352 × 310 pixels. The solidified droplet's surface morphology and elemental distribution were analyzed using a Zeiss EVO10 scanning electron microscope (SEM) (Carl Zeiss AG, Germany) equipped with energy-dispersive x-ray spectroscopy (EDS) detectors. Furthermore, ImageJ (https://imagej.net/), an image analysis software [48], was utilized to measure the characteristic dimensions of the droplets.

3. Results and discussion

3.1. *Aluminum droplet ejection under coaxial shielding gas*

The stable ejection of droplets is fundamental to achieving high-

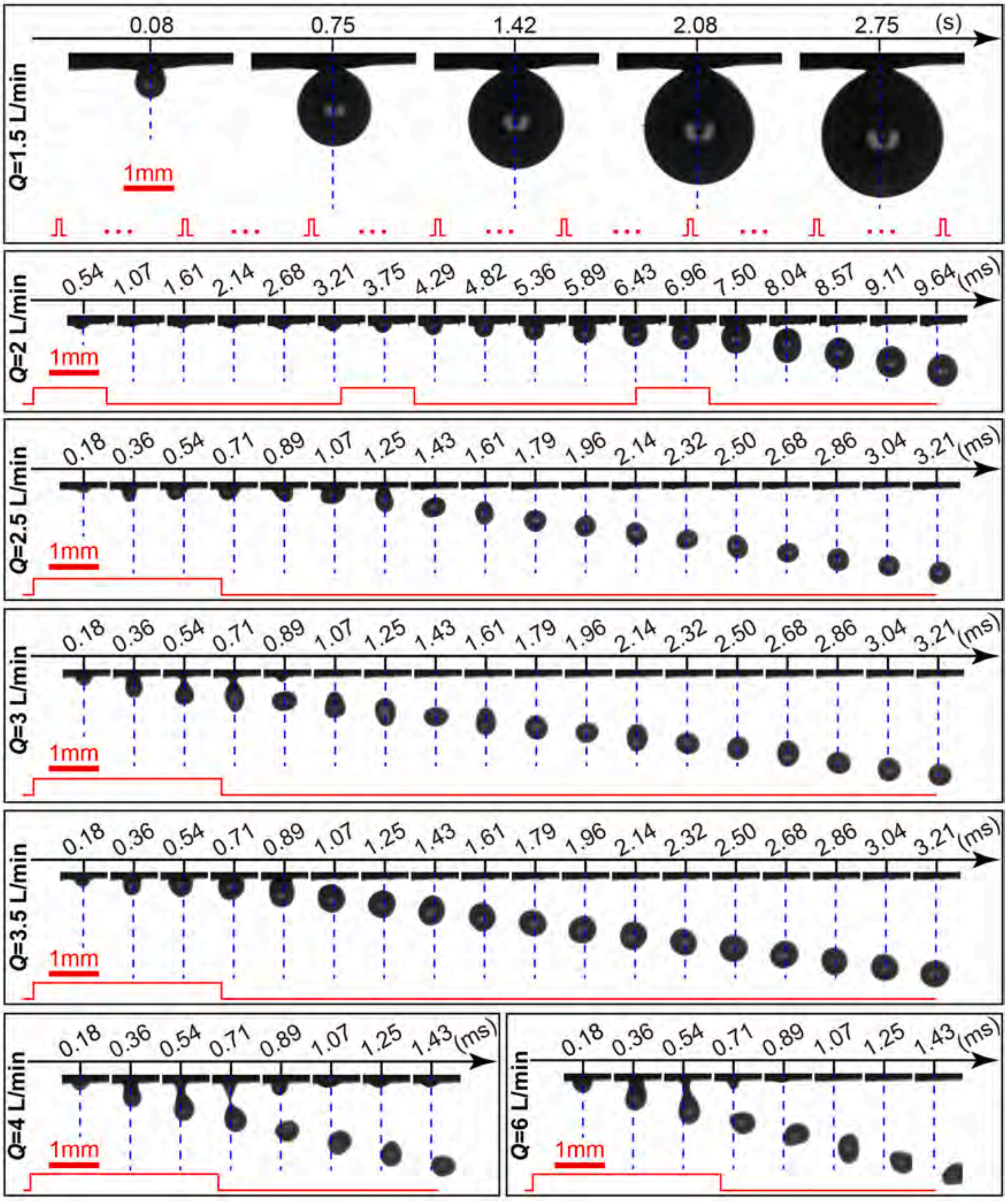

Fig. 3. CCD snapshots of the aluminum droplet ejection process at different shielding gas supply rates (1.5–6 L/min). The red staircase solid line indicates the applied piezoelectric driving waveform, and the blue dashed line marks the nozzle central axis.

precision deposition. In the droplet ejection experiments, the heating furnace temperature was maintained at 1023 K, ensuring the complete melting of the aluminum alloy within the crucible. A nozzle with a diameter of 500 μm was used, and key process parameters were held constant: voltage at 4.5 V, pulse width at 698 μs, and backpressure at 0 kPa.

During ejection, when the pulse signal is high, the forward motion of the vibration rod increases the pressure at the nozzle outlet, generating a metal jet. When the pulse signal returns low, the backward motion of the vibration rod creates a velocity difference between the head and the root of the jet, leading to jet necking and breakup. In this process, the metal jet must overcome surface tension and viscosity to ultimately form a single metal droplet [30]. In this study, jet breakup is primarily driven by inertial forces. This is indicated by a Weber number (*We*) of approximately 10, defined as $We = \rho_L v_{jet}^2 d_n / \sigma$, where v_{jet} is the initial jet velocity and d_n is the nozzle diameter. Given that droplet breakup occurs at the nozzle outlet and that the ejection dynamics are governed by the jet formation process, it is therefore appropriate to use the nozzle diameter (d_n) as the characteristic length. The obtained Weber number indicates that inertia dominates over surface tension during droplet formation.

At low shielding gas supply rates, the formation of an oxide film on the droplet surface significantly alters its physical properties. Xu et al. [49] used the pendant drop method to measure the surface tension of gallium metal droplets, demonstrating that self-limiting oxides generate yield stresses, thereby increasing the measured surface tension. Similarly, the oxide film impacts the apparent viscosity of metallic fluids. Investigations by Xu et al. [49] on molten gallium and by Patouillet et al.

[38] on aluminum alloys have shown that oxidation induces a non-Newtonian, shear-thinning behavior in the melt surface. In this case, the surface viscosity decreases with increasing shear rate due to continuous oxide film rupture. As the shear rate increases, the oxidized melt's high viscosity approaches that of pure metal. Zhou et al. [50] further explored the effects of oxidation on the ejection of tin alloy droplets, finding that the self-limiting oxide film inhibits the release of surface energy during jet necking. As a result, tin alloy droplets exhibit a characteristic tapered tail. According to existing research, the parabolic rate constants for oxide film growth on tin alloy droplets at working temperatures of 523–623 K range from 2.793×10^{-23} to 4.426×10^{-22} m^2/s [35]. For aluminum alloy droplets at 1023–1123 K, the values ranges from 5.669×10^{-19} to 2.275×10^{-17} m^2/s [36]. This indicates a 3–6 orders of magnitude increase, leading to significantly differences in their ejection and breakup dynamics.

Fig. 3 presents CCD snapshots of aluminum alloy droplet ejection at different shielding gas supply rates. At a low shielding gas supply rate (Q) of 1.5 L/min, a hanging-drop phenomenon is observed due to severe surface oxidation. The dense and chemically stable oxide film formed on the aluminum droplet inhibits normal jet breakup. Even with an increase in the number of pulse signals, the initial kinetic energy of the metal jet remains insufficient to overcome the surface tension and viscosity of the oxidized melt. This leads to the accumulation of a hanging drop at the nozzle outlet and causing a blockage. As the shielding gas supply rate increases to 2.5 L/min, oxidation is reduced, and the hanging-drop effect is eliminated. The required number of pulses to generate a single droplet decreases to one. However, when the shielding gas supply rate exceeds 4 L/min, the droplet is accelerated by the shielding gas dynamics, causing its trajectory to deviate from the central axis of the metal jet (see blue dashed line in Fig. 3). This indicates excessive shielding gas flow compromises the ejection accuracy of aluminum droplets. Optimal ejection conditions are achieved at shielding gas supply rates between 3 and 3.5 L/min. Under these conditions, normal jet breakup and precise single-droplet formation are obtained. To ensure stable droplet ejection during the aluminum deposition process, the shielding gas flow rate was maintained at 3.2 L/min in all subsequent experiments.

The visual presentation of the aluminum alloy droplet ejection process under different shielding gas supply rates is shown in Supplementary Video 1.

3.2. Aluminum droplet deposition under coaxial shielding gas

3.2.1. Dynamics of the metal droplet deposition process

The deposition process of aluminum alloy droplets onto a substrate is influenced by the interplay of dynamic and thermodynamic behaviors. This process can be divided into four stages: spreading, recoil, oscillation, and stationary. During the spreading stage, the droplet falls and comes into contact with the substrate surface. The internal fluid continues to move downward due to inertial forces, causing its height to decrease and its width to increase. The spreading ceases when the initial kinetic energy is sufficiently dissipated through viscous and possible solidification effects. At this point, surface tension forces balance the residual kinetic energy, resulting in an equilibrium shape. Previous studies [31,51,52] have demonstrated that the maximum spreading ratio of molten droplets is closely related to solidification behavior dominated by droplet and substrate temperatures. Predictive models have been developed on this basis. In this work, since the droplet temperature and substrate temperature remained constant, the influence of solidification on droplet spreading was not considered. In the recoil stage, the droplet recoils upwards due to surface tension, gradually regaining height. As partial solidification begins from the bottom up, the spreading diameter contracts slightly. Meanwhile, the unsolidified portion continues to recoil upwards. The droplet's kinetic energy is converted into surface energy until it reaches the maximum recoil height. During the oscillation stage, the droplet oscillates with progressively diminishing amplitude as it seeks to balance the remaining kinetic and surface energies. Finally, in the stationary stage, the droplet fully solidifies and comes to rest.

During the droplet's flight and falling, its thermal energy is primarily transferred to the atmosphere through thermal convection and thermal radiation. The cooling rate of the droplet can be approximated using Newton's law of cooling as [53]

$$\frac{dT_d}{dt} = -\frac{6\left[h\left(T_d - T_g\right) + \sigma_{SB}\varepsilon_e\left(T_d{}^4 - T_g{}^4\right)\right]}{\rho_L C_L D_d}, \tag{2}$$

where T_d and T_g are the initial temperatures of the droplet and the shielding gas environment; ρ_L, C_L, D_d, and h are the droplet density, specific heat, diameter, and convective heat transfer coefficient, respectively; σ_{SB} is the Stefan-Boltzmann constant, which is 5.67×10^{-8} $W \cdot m^{-2} \cdot K^{-4}$; ε_e is the emissivity. The convective heat transfer coefficient h could be obtained from the Ranz-Marshall equation [54]

$$h = \frac{k_g}{D_d}\left(2 + 0.6 Re_g{}^{1/2} Pr_g{}^{1/3}\right). \tag{3}$$

Re_g is the Reynold number of shielding gas, defined as $Re_g = |v_g - v_d| D_d \rho_g / \mu_g$; Pr_g is the Prandtl number of shielding gas, expressed by $Pr = C_g \mu_g / k_g$; ρ_g, k_g, μ_g, v_g, and C_g are the density, thermal conductivity, viscosity, velocity, and specific heat of the shielding gas, respectively. During the experiment, the initial temperatures of the droplet and the inert atmosphere are 1023 K and 350 K, respectively. The droplet has a diameter of approximately 560 μm and the shielding gas velocity does not exceed 6 m/s. Based on these conditions, the convective heat transfer coefficient is estimated to be approximately 274.81 $W \cdot m^{-2} \cdot K^{-1}$. Even assuming the emissivity is at its maximum value of 1, the droplet's cooling rate would not exceed -1008.9 $K \cdot s^{-1}$. Given that the droplet flight time is less than 7 ms, the corresponding temperature variation is estimated to be less than 7.122 K. This results in a temperature variation rate below 0.72 %. These results suggest that the temperature change during droplet flight could be negligible.

Once the droplet has fully detached from the nozzle surface, it begins to fall freely with a certain initial velocity. During this process, the droplet's motion is primarily governed by the gravitational forces and the drag force exerted by the shielding gas. A dynamic model describing the droplet's flight could be derived using Newton's second law of motion as [55]

$$\frac{1}{6}\pi D_d{}^3 \rho_L \frac{dv_d}{dt} = \frac{1}{6}\pi D_d{}^3 \rho_L g - \frac{1}{8} C_{drag} \pi D_d{}^2 \rho_g \left|v_d - v_g\right| \left(v_d - v_g\right), \tag{4}$$

where ρ_d and v_d represent the density and velocity of molten droplets; C_{drag} is the drag force coefficient of shielding gas, which could be calculated by $C_{drag} = 24/Re_g{}^{0.646}$ [56]. Thus the droplet's falling acceleration could be given by

$$\frac{dv_d}{dt} = g - \frac{3 C_{drag} \rho_g}{4 D_d \rho_d} \left|v_d - v_g\right| \left(v_d - v_g\right). \tag{5}$$

Calculations show that during a maximum flight time of 7 ms, the droplet's acceleration would not exceed 23.555 $m \cdot s^{-2}$. This value is higher than gravitational acceleration because of the extra momentum imparted by the coaxial shielding gas. In this case, the increase in the droplet velocity would remain below 0.166 m/s, suggesting that the influence of droplet velocity variations on the deposition process could be neglected.

3.2.2. Effect of deposition distance on droplet deposition behaviors

The process parameters play a critical role in governing the oxidation and dynamics of droplets during deposition. Previous studies have demonstrated that the bonding between droplets and the substrate is significantly affected by the substrate temperature. Low substrate temperature can cause droplet rebound [57], whereas moderately

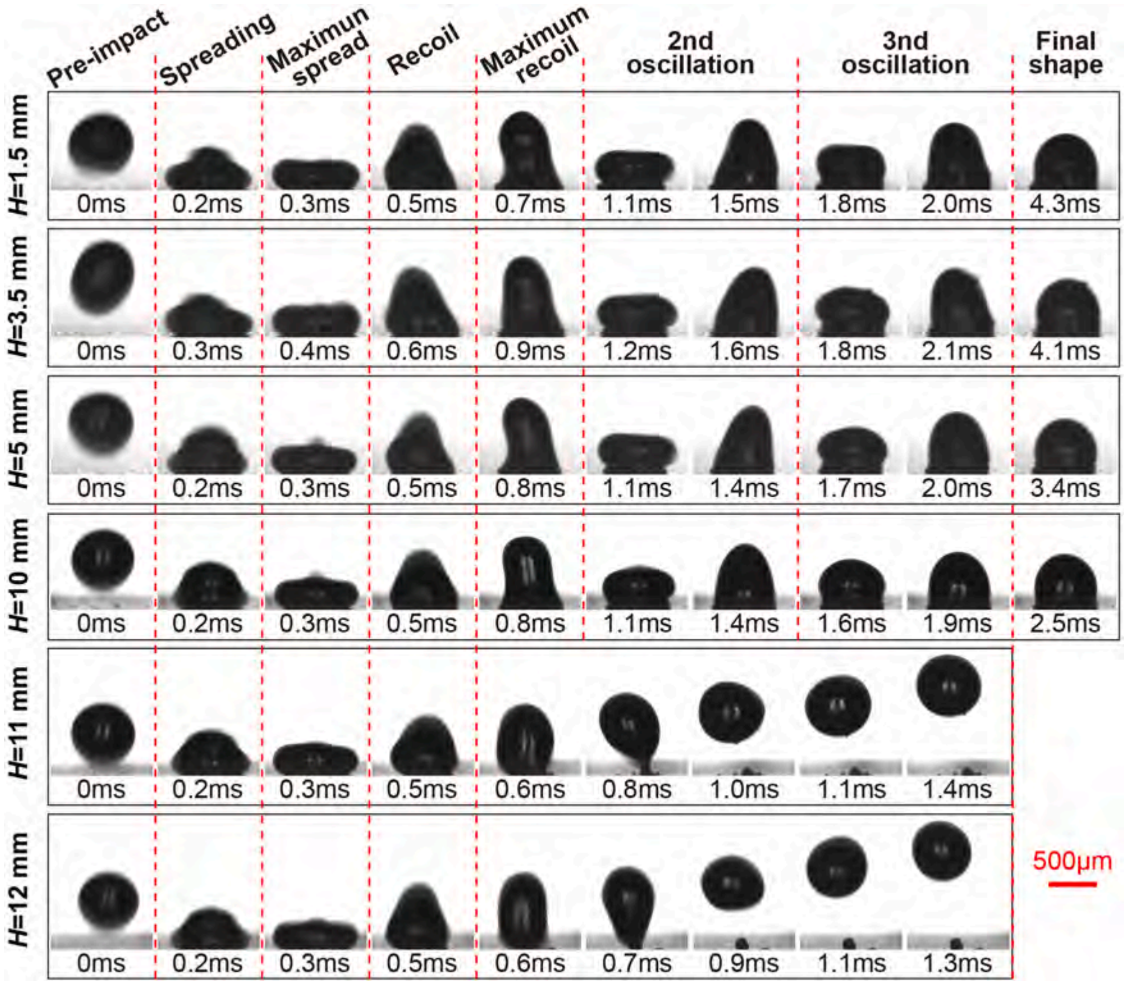

Fig. 4. CCD snapshots of the aluminum droplet deposition process at different deposition distances (1.5–12 mm). The sequential images record the evolution from Pre-impact to the final rest, and the shielding gas supply rate was maintained at 3.2 L/min.

increasing the substrate temperature enhances the pinning effect between the droplets and the substrate [58]. In this study, the substrate temperature was set at 573 K to avoid rebound caused by insufficient substrate temperature.

Different deposition distances ranging from 1.5 mm to 12 mm were set for the experiment. Fig. 4 illustrates the deposition behavior of aluminum alloy droplets at varying distances. When the deposition distance H is less than 3.5 mm, droplets undergo normal spreading, recoil, oscillation, and eventually reach a stationary state. The stabilization requires at least 4 ms after droplet-substrate contact. When the deposition distance increases to 10 mm, the time required for stabilization is almost halved. In principle, as the deposition distance increases, the time required for the droplet to reach a stationary state should also increase. However, Fig. 4 shows the opposite trend. This phenomenon is attributed to oxidation behavior in this study. Specifically, as the deposition distance increases, droplet oxidation is enhanced. The oxidized surface introduces local viscoelastic or shear-dependent resistance during oscillation. For deposition distances exceeding 11 mm, aluminum alloy droplets begin to rebound upon contacting the substrate. This results from oxide film formation, affecting the wetting or adhesion between the droplet and the substrate. The detailed mechanism of oxidation effects will be discussed in the following sections.

To quantitatively analyze droplet vertical dynamics during deposition, the droplet recoil factor, $\eta(t)$, was used. This parameter is defined as the ratio of the liquid surface height, $h(t)$, to the initial droplet diameter, D_d, and is expressed mathematically as $\eta(t) = h(t)/D_d$. The temporal variation of $\eta(t)$ was statistically analyzed using the moment of droplet-substrate contact as the initial time point. The results are shown in Fig. 6. Notably, Fig. 6 represents the temporal evolution of the recoil factor for a single droplet deposition event, extracted from Fig. 4. During the spreading stage, the curves' slopes for different deposition distances exhibit minimal variation, indicating that changes in the droplets' initial impact velocity could be neglected. During the recoil stage, except for droplets that rebounded at the deposition distances of $H \geq 11$ mm, the maximum recoil factor decreases slightly as the deposition distance increases. During the oscillation stage, both the amplitude and period of droplet oscillations significantly decrease as H increases from 3.5 mm to 10 mm. As a result, droplets reach a stationary state more quickly.

Since variations in droplet velocity and temperature during flight are minimal, the observed changes in oscillation behavior are most likely attributed to oxidation effects. Deposition distance plays a critical role in determining oxygen exposure during droplet flight and impact. As the gas travels downward from the nozzle, it entrains ambient air due to turbulent mixing. The degree of inert gas dilution and the local oxygen concentration near the droplet are strongly influenced by the axial distance from the nozzle. The concentration decay model of shielding gas, proposed by Dowling et al. [59], could be adopted to analytically describe this behavior. Their experimental work demonstrated that the concentration field of gas-phase jets follows a self-similar profile, with the axial and radial concentration distribution described by:

$$C(x,r) = \frac{\varphi C_0 d^*}{x - x_0}\cdot g\left(\frac{r}{x - x_0}\right), \tag{6}$$

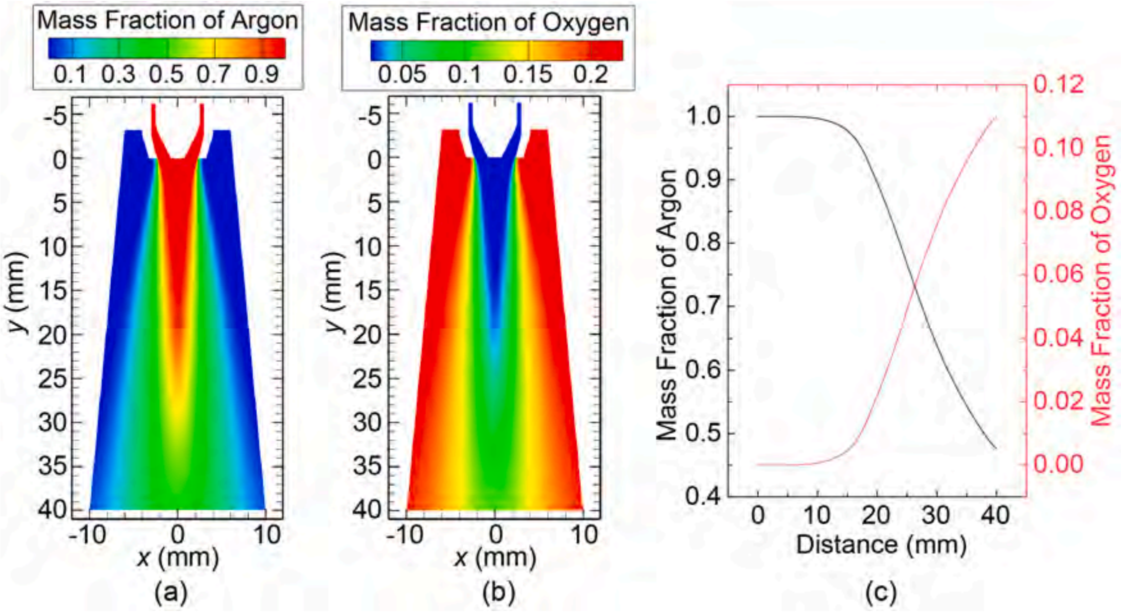

Fig. 5. Numerical simulation for gas concentration: (a) Distribution of argon mass fraction; (b) Distribution of oxygen mass fraction; (c) Variation of argon and oxygen concentrations along the nozzle axis.

where $C(x, r)$ is the inert gas concentration at axial distance x and radial distance r; φ is an empirical constant; C_0 is the jet exit concentration; d^* is the momentum diameter of the nozzle exit; x_0 is the virtual origin of the jet flow; $g(n)$ is a smooth function that has a maximum value of $g(0) = 1$ and is determined experimentally. Although the Dowling' entrainment model assumes free jet conditions, its qualitative applicability is supported by studies on confined annular jets and plumes. Experimental investigations of confined coaxial jets have shown that centerline concentration decay persists despite near-field confinement [60], while simulations of confined coannular jets further confirm consistent concentration attenuation behavior [61,62]. According to Eq. (6), the centerline concentration of inert gas decreases inversely with distance from the nozzle due to entrainment and mixing with ambient air. To further verify the observation, a numerical simulation was conducted based on the k–ε turbulence model and the non-reacting species transport model, as shown in Fig. 5. The results present the distribution of argon mass fraction (Fig. 5a) and oxygen mass fraction (Fig. 5b) near the nozzle outlet. Fig. 5c illustrates the variation of argon and oxygen concentrations along the nozzle axis. The results clearly show that the argon concentration decreases with increasing distance from the nozzle. At the same time, the oxygen concentration increases gradually. This observation provides further confirmation of the reliability of the present analysis.

Consequently, as the deposition height H increases, the droplet travels through a longer shielding gas atmosphere, where more ambient air becomes entrained. This raises oxygen concentration near the substrate. In addition, longer droplet flight times further prolong oxygen exposure, enhancing the likelihood of partial surface oxidation. The time scale of the droplet oscillation period could be estimated using the following expression [63]:

$$t_{\mathrm{osc}} \approx 2.3\sqrt{\frac{\rho_{\mathrm{L}} {D_{\mathrm{d}}}^{3}}{8\sigma}}, \tag{7}$$

where σ represents the surface tension of aluminum droplets. For non-oxidized droplets, t_{osc} is approximately 0.576 ms. However, for oxidized droplets, the oscillation period would decrease as oxidation elevates the equivalent surface tension of metal droplets [49]. This shortens the time required for the droplet to reach a stationary state, as

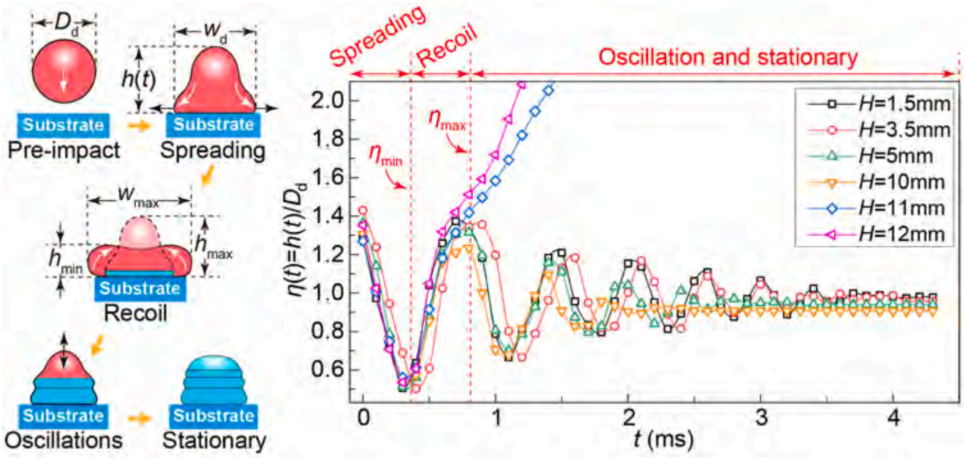

Fig. 6. Temporal variation of the recoil factor of aluminum alloy droplets for different deposition distances ranging from 1.5 to 12 mm, sampled from the deposition process shown in Fig. 4.

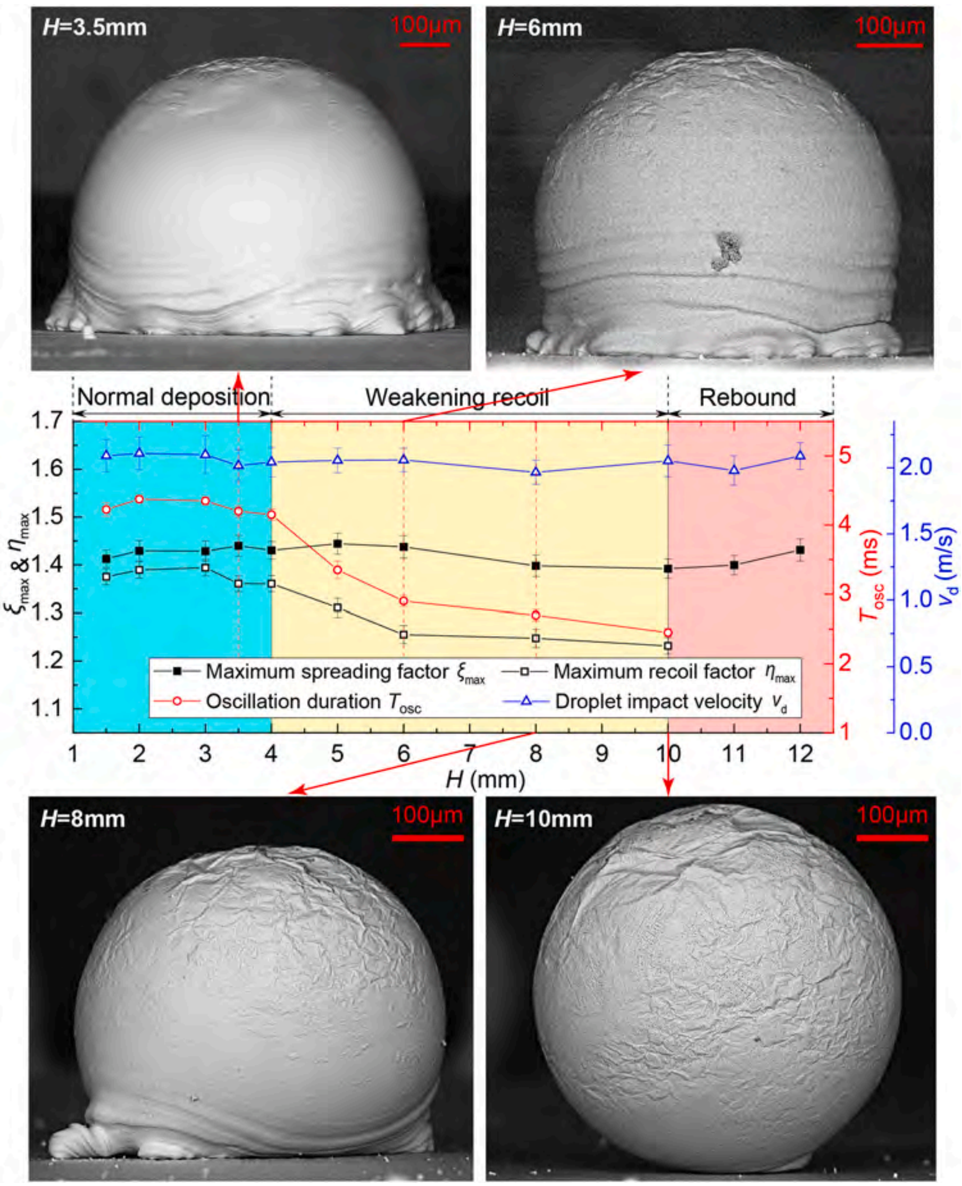

Fig. 7. Variation of droplet characteristic parameters, including maximum spreading factor, maximum recoil factor, oscillation duration, and impact velocity, and final solidification morphology with deposition distances. Each data point represents the average of 15 droplets.

observed in the variation of $\eta(t)$ for deposition heights less than 10 mm in Fig. 6. Meanwhile, with increasing oxidation levels, the droplet surface is covered by progressively thicker oxide layers. While molten aluminum itself exhibits Newtonian behavior, the presence of surface oxides may introduce localized viscoelastic or shear-dependent resistance [37]. This leads to notable dampening of oscillatory motion. Moreover, the in-flight oxidation can also form a thin oxide film on the droplet surface before impact, which may reduce wettability upon contact. Aluminum droplets are highly sensitive to atmospheric oxygen content. As oxygen levels increase, even if a dense oxide film does not form during the brief deposition interval, discrete oxide particles or "oxide islands" may develop [64]. The reduced wettability and the discrete alumina particles hinder the bonding between droplet and substrate, ultimately resulting in droplet rebound. This can be seen in the variation of $\eta(t)$ for deposition heights greater than 10 mm in Fig. 6.

The visual presentation of the aluminum droplet deposition process under different deposition distances is shown in Supplementary Video 2.

3.2.3. *Effect of deposition distance on droplet oxidation morphology*

To further substantiate the oxidation of droplets during the deposition process, a detailed analysis of their final printed morphology was conducted. In addition to the droplet recoil factor (η), the droplet spreading factor (ξ) is another critical dimensionless parameter for describing the droplet impact. It is defined as the ratio of the liquid surface width (w_d) to the initial droplet diameter (D_d) as $\xi = w_d / D_d$. Fig. 7 presents the variation in key droplet characteristics, including the maximum spreading factor (ξ_{max}), maximum recoil factor (η_{max}), oscillation duration (T_{osc}), and impact velocity (v_d) at different deposition distances, alongside with their corresponding solidified morphologies. Each data point represents the mean value of 15 droplets. The impact velocity and the maximum spreading factor remain relatively constant across deposition distances. However, the maximum recoil factor and oscillation duration exhibit significant changes that follow a similar trend. Based on these observations, the droplet deposition process could be classified into three distinct regimes: normal deposition, weakened recoil or oscillation, and rebound. For deposition distances of less than 4 mm, aluminum droplets exhibit normal and consistent deposition

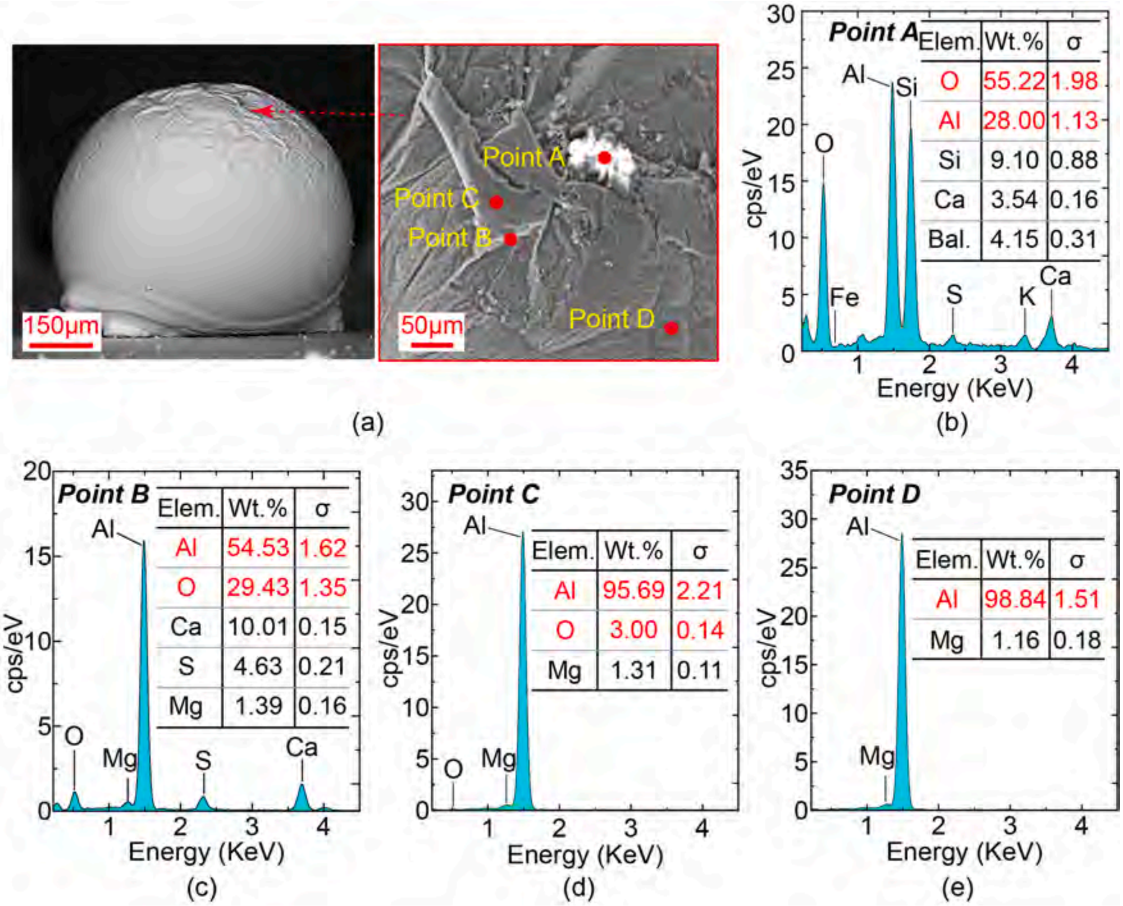

Point A

Elem.	Wt.%	σ
O	55.22	1.98
Al	28.00	1.13
Si	9.10	0.88
Ca	3.54	0.16
Bal.	4.15	0.31

Point B

Elem.	Wt.%	σ
Al	54.53	1.62
O	29.43	1.35
Ca	10.01	0.15
S	4.63	0.21
Mg	1.39	0.16

Point C

Elem.	Wt.%	σ
Al	95.69	2.21
O	3.00	0.14
Mg	1.31	0.11

Point D

Elem.	Wt.%	σ
Al	98.84	1.51
Mg	1.16	0.18

(a) (b) (c) (d) (e)

Fig. 8. (a) Localized secondary electron scanning morphology of the droplet's top surface wrinkles. (b-e) EDS analysis results corresponding to points A, B, C, and D, respectively.

behavior. At deposition distances of 4–10 mm, the recoil height and the oscillation duration decrease substantially. SEM images show that as the deposition distance increases, the weakening of the oscillation results in fewer oscillation ripples and wrinkle-like surface morphologies. Initially, these wrinkles appear only at the apex of the droplets at shorter distances, but gradually extend over the entire droplet surface as the distance increases.

The formation of surface wrinkles on the droplet could be explained through oxidation theory. Nayebi et al. [65] investigated the oxidation of molten aluminum and reported that the oxide films formed in atmospheric conditions exhibit non-uniform, wrinkled, and sometimes torn morphologies. Oxide films induce stress concentrations on the metal surface, which primarily originating from two sources: growth stress and thermal stress. Growth stress is predominantly influenced by the Pilling-Bedworth Ratio (*PBR*), which is a critical dimensionless parameter used to assess the stress state within the oxide film. The *PBR* is defined as the volume ratio of the oxide to the metal consumed during oxide formation and is expressed as:

$$PBR = \frac{M_{\text{oxide}}\rho_{\text{metal}}}{nM_{\text{metal}}\rho_{\text{oxide}}} \tag{8}$$

where M_{metal} and M_{oxide} represent the mole masses of the metal and its oxide, respectively; n is the number of metal atoms in one molecule of the oxide; ρ_{metal} and ρ_{oxide} are the densities of the metal and its oxide, respectively. The oxide film experiences compressive stress when the *PBR* is greater than 1, and tensile stress when the *PBR* is less than 1. For aluminum oxide, the *PBR* is approximately 1.29 [66], indicating that a larger volume of alumina is formed than the volume of aluminum consumed. This volumetric expansion induces compressive stress within the oxide film, potentially compromising its integrity and stability. Additionally, thermal stress arises due to differences in the solidification contraction coefficients between the metal and its oxide film. Pure aluminum has a linear thermal expansion coefficient of $\sim 23.8 \times 10^{-6}$ K^{-1} [67] and a relatively high solidification shrinkage coefficient of 3.5~7.8 % [68]. In contrast, the alumina layer, as a ceramic material, exhibits a much lower thermal shrinkage or expansion behavior, with a linear thermal expansion coefficient of $\sim 8 \times 10^{-6}$ K^{-1} [69]. During solidification, the mismatch in contraction coefficients generates contraction stresses, deforming the oxide film and formatting surface wrinkles [65]. Jiang et al. [70] conducted a systematic study on the oxidation of 6061 aluminum alloy, finding that increased oxidation time causes higher surface roughness and thicker oxide layers. This reinforces the idea that surface topography, especially wrinkling or roughening, can reflect the extent of oxidation, even if not chemically quantitative.

To further probe wrinkling, the thermal solidification dynamics of the aluminum alloy droplet were analyzed. Upon substrate contact, the droplet solidifies at the bottom first. During the bottom-up solidification, the movement of the solidification front can be approximated using a Neumann-type solution of the Stefan problem. Assuming that the droplet undergoes one-dimensional heat diffusion in the longitudinal direction, the solidification front position $s(t)$ are given by [71]:

$$s(t) = 2\lambda\sqrt{\alpha t} \tag{9}$$

where α is the thermal diffusivity of aluminum, which can be calculated by $\alpha = k_S/(\rho_S C_S)$. λ is a constant derived from the Stefan number. By taking the derivative of Eq. (9), the moving velocity of the droplet solidification front, $v_f(t)$, can be expressed as:

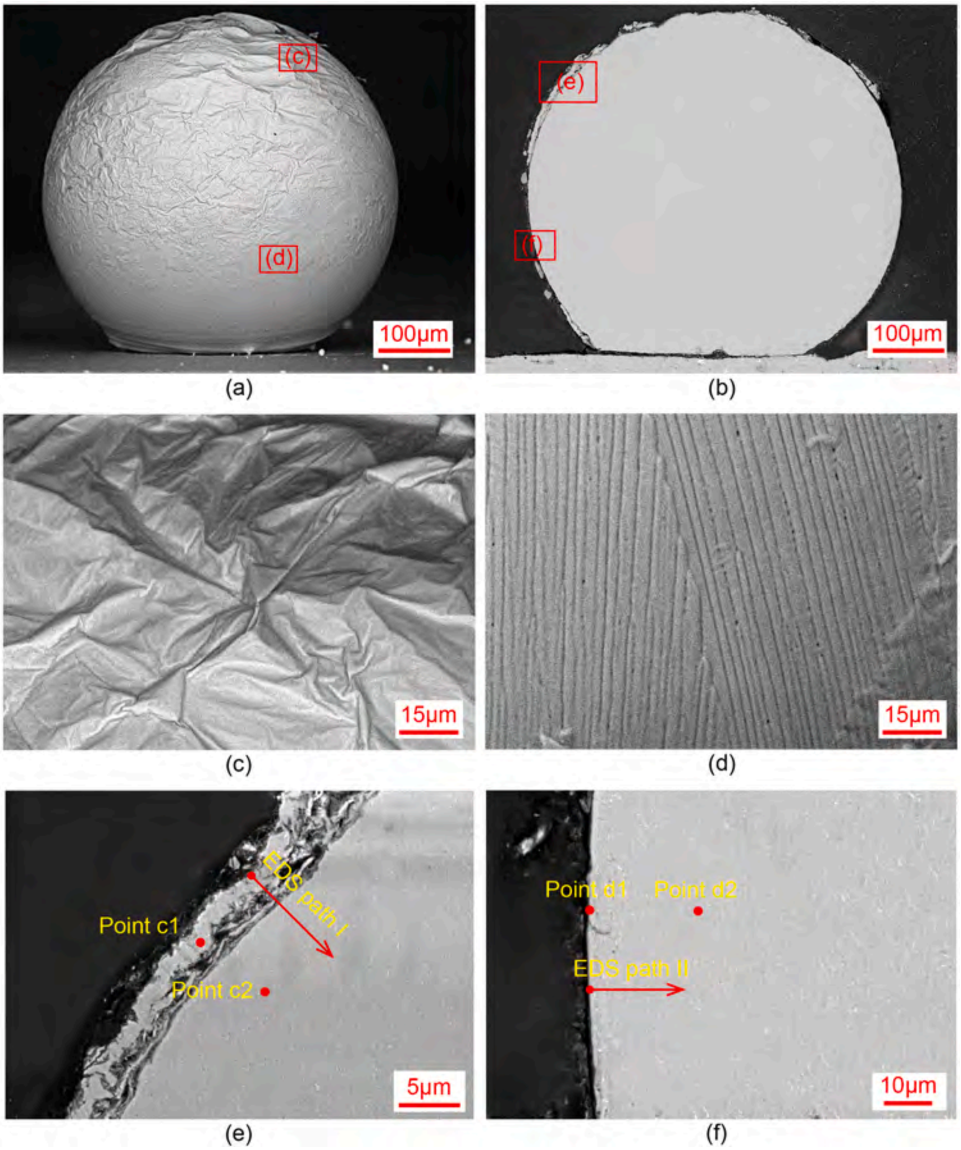

Fig. 9. (a) SEM morphology of the droplet at the deposition distance of 9.5 mm. (b) Internal cross-section SEM morphology for the droplet in (a). (c) Magnified view of the top wrinkle region in (a). (d) Magnified view of the bottom smooth region in (a). (e) Droplet local SEM morphology on the top edge. (f) Droplet local SEM morphology on the middle edge.

$$v_f(t) = \lambda\sqrt{\frac{\alpha}{t}}. \tag{10}$$

This expression indicates that the solidification front velocity is highest at the bottom of the droplet and gradually decreases toward the top, meaning that the upper region solidifies more slowly. Both uneven cooling and oxidation may contribute to the non-uniform distribution of wrinkles. However, experimental observations consistently show that wrinkling occurs predominantly on the top surface rather than at the rapidly solidifying bottom. This suggests that the wrinkling is not primarily governed by differential thermal shrinkage caused by solidification speed variations. If the thermal contraction were dominant, the bottom, where cooling is faster would exhibit more severe wrinkling, which contradicts the experimental results. Instead, the wrinkle distribution variation likely arise from oxidation duration differences. During delayed solidification at the top region, prolonged oxygen exposure forms a relatively thick and rigid oxide layer. This oxide film, mechanically constrained by the underlying alloy that continues to shrink during solidification, experiences compressive stress due to thermal mismatch and restricted volume contraction. The resulting instability causes the oxide layer to buckle, producing visible wrinkles. Therefore, the observed non-uniform wrinkle morphology can be attributed to the combined effects of uneven cooling and oxidation, with oxidation-induced compressive stress playing the dominant role.

Notably, the solidification of the droplet initiates from the bottom, which is in direct contact with the substrate and remains mechanically constrained throughout the cooling process. This constraint restricts the macroscopic dimensional shrinkage at the droplet base, especially the radial contraction. As a result, while the bottom diameter is effectively "locked", the upper portion of the droplet continues to thermal shrink freely, and generates wrinkled morphology when severely oxidized. Fig. 8a shows the localized secondary electron scanning morphology of wrinkles at a deposition distance of 8 mm. White bright spots have been observed in the wrinkle aggregation area. Due to the low conductivity of alumina, more charges accumulate on the oxide, making it appear whiter than the aluminum matrix under SEM. To further investigate the formation mechanism of surface wrinkles on aluminum droplets, EDS analysis was conducted on the local wrinkles. The EDS sampling locations are shown in Fig. 8a, where point A is the location of the white bright spot, point B is at the wrinkle crease, point C is on the flat part of

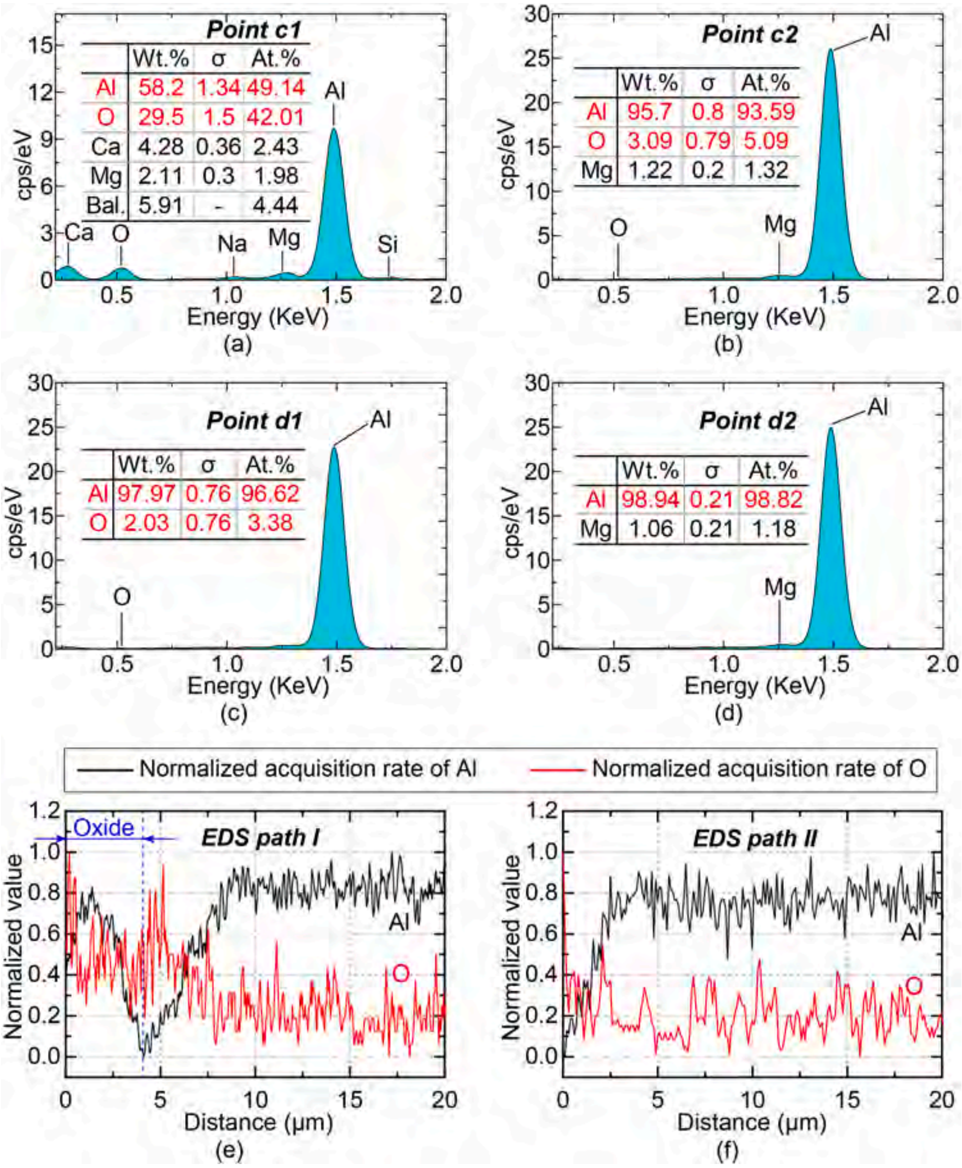

Point c1

	Wt.%	σ	At.%
Al	58.2	1.34	49.14
O	29.5	1.5	42.01
Ca	4.28	0.36	2.43
Mg	2.11	0.3	1.98
Bal.	5.91	-	4.44

Point c2

	Wt.%	σ	At.%
Al	95.7	0.8	93.59
O	3.09	0.79	5.09
Mg	1.22	0.2	1.32

Point d1

	Wt.%	σ	At.%
Al	97.97	0.76	96.62
O	2.03	0.76	3.38

Point d2

	Wt.%	σ	At.%
Al	98.94	0.21	98.82
Mg	1.06	0.21	1.18

Fig. 10. (a-d) EDS point analysis for sampling points in Fig. 9e,f. (e-f) Distribution data for Al and O for sampling lines in Fig. 9e,f.

the wrinkle surface, and point D is on a flat area away from the dense wrinkle region. Fig. 8b-e present the EDS analysis results corresponding to points A, B, C, and D, respectively. Extremely high O content was detected at the white bright spot location and the crease location of the wrinkles, while relatively lower O content was found at the flatter regions. The differences in oxygen content observed can be attributed to the heterogeneous nucleation of oxide formation on aluminum alloy surfaces. Aluminum droplet oxidation behavior follows a typical island nucleation and lateral growth mechanism, widely reported in fundamental studies [72–75]. Nucleation sites include grain boundaries (due to irregular atomic arrangement and higher chemical activity), scratches or damage, second-phase particles, and zones of residual stress. Oxidation starts with scattered oxide islands, which gradually grow and coalesce. This non-uniform initiation explains the localized oxygen enrichment observed on droplet surfaces. Point A lies in a prominent wrinkle region where accumulated oxide islands may coalesce, forming a locally thicker oxide layer that results in higher O content. Point B, situated within a crease or fold, exhibits complex geometry with elevated surface roughness and potential micro-cracks. These characteristics increase the effective reactive surface area and may facilitate localized oxygen adsorption or retention by oxide particles. Points C and D reside on smoother, flatter surface regions. These areas have fewer oxidation nucleation sites and lower surface energy, leading to reduced oxidation and consequently lower measured O content.

Fig. 9 presents the external (Fig. 9a) and internal (Fig. 9b) cross-sectional morphology of a severely oxidized droplet at a deposition distance of 9.5 mm. The wrinkling on the droplet surface is most pronounced near the top, as shown in Fig. 9c. The wrinkle density gradually decreases towards the bottom, where the surface remains comparatively smooth (Fig. 9d). A distinct boundary layer is also observed in the upper part of the droplet. This features a relatively loose and irregular edge on its outer side and a more uniform and dense aluminum alloy structure on its inner side, as depicted in Fig. 9e. In the lower part of the droplet, the boundary layer is significantly less pronounced, with the droplet displaying a sharp and clear edge morphology, as shown in Fig. 9f. EDS analyses were conducted at different locations on the droplet shown in Fig. 9e,f. Sampling points c1 and d1 were selected at the boundary layer and the droplet edge. Points c2 and d2 were chosen inside the droplet, away from the edge. Scanning lines I and II both start from the outermost edge of the droplet and proceed inward. The EDS analysis results are presented in Fig. 10. Specifically, Fig. 10a-d correspond to the EDS point analysis results for sampling points c1, c2, d1, and d2, respectively. It is

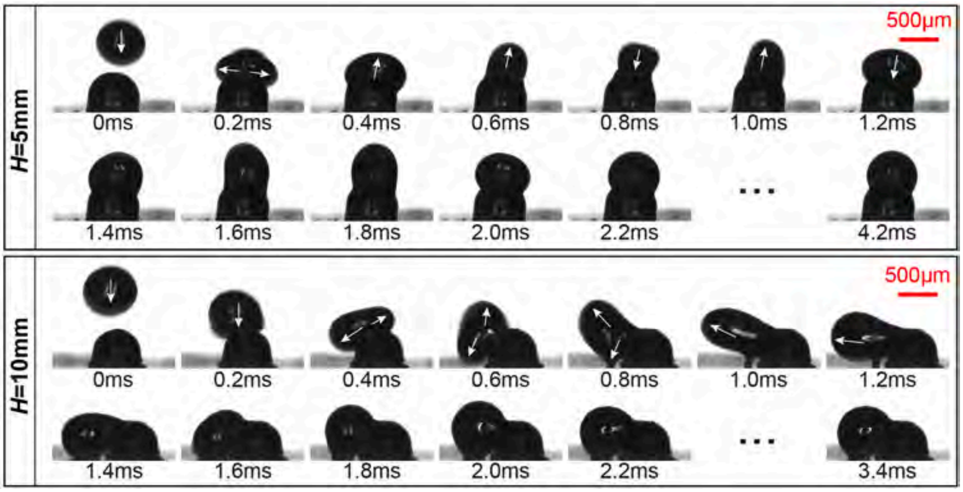

Fig. 11. Pile-up process of droplets with different oxidation levels.

evident that a higher O content was detected at point c1 on the droplet boundary layer, while other sampling points exhibited lower oxygen O content. Fig. 10e,f present the EDS line scan results for scanning lines I and II, respectively. A region of higher O content distribution was detected along the irregular boundary layer of the droplet. By contrast, no significant O enrichment is observed at the sharper edge, indicating that the droplet irregular boundary layer is primarily composed of oxides. High-temperature oxide films typically have micro-cracks or defects, and alumina is renowned for its high hardness and inherent brittleness. During the grinding and polishing process, mechanical stress can cause localized deformation or peeling of the oxide film. This results in the formation of a loose and separated boundary layer.

Notably, the oxide layer shown in Fig. 9e appears thicker than typical native oxide films formed on aluminum surfaces. Native Al_2O_3 films are

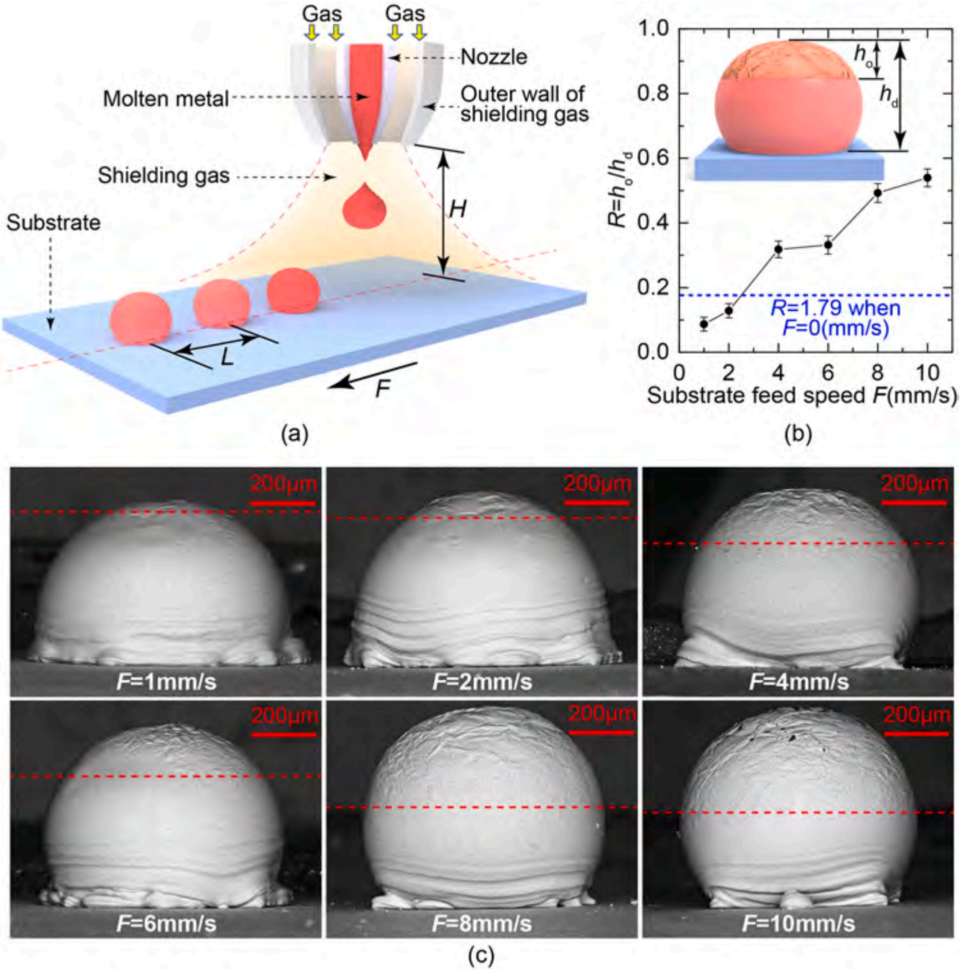

Fig. 12. (a) Schematic diagram of droplet printing. Variation of (b) droplet wrinkle index and (c) deposition morphology under different substrate feed speeds.

usually below 1 μm under normal conditions. However, prior studies show that molten aluminum in oxygen-rich environments can form much thicker layers. Yang et al. [41] reported that aluminum droplets exposed to 100,000 ppm oxygen exhibited oxide film up to 1.4 μm thick. This indicates that rapid oxidation during droplet spreading can lead to substantial oxide accumulation. Similarly, Salas et al. [73] observed that oxide layers with several microns of thickness can develop on molten aluminum surfaces, especially when wrinkles or multilayer oxides formed. In this study, the region examined in Fig. 9e corresponds to a heavily wrinkled area. Folded oxide layers and localized oxygen enrichment may result in a multilayered or non-uniform oxide zone, contributing to the observed apparent thickness. The element co-presence of Ca and O in this region also warrants discussion. Although Ca is not a major component of 6061 aluminum alloy, Bergsmark et al. [76] reported that trace Ca in impurities can migrate to the oxidized surface of molten aluminum via grain boundary or surface diffusion, similar to Mg. Given Ca's strong affinity for O, localized enrichment of CaO may occur, especially near surface defects. In this study, the Ca signal may also stem from residual contamination or environmental sources. Such effects could further enhance Ca presence in highly oxidized and structurally complex regions.

Although the droplet may maintain good ejection accuracy at varying deposition distances, the presence of a surface oxide layer could negatively impact the bonding between successive droplets, thereby affecting the accuracy of subsequent droplet deposition. Fig. 11 illustrates this effect by comparing droplets deposited at 5 mm and 10 mm distances in a pile-up study. These two distances represent different levels of oxidation. At a 5 mm deposition distance, droplet oxidation is minimal. The second droplet is likely to induce partial remelting or enhanced wetting of the first droplet. This promotes proper adhesion on the top of the first droplet. Conversely, at a deposition distance of 10 mm, droplet oxidation is more pronounced. The second droplet fails to properly pile up after contacting the first. The oxide layer not only shortens the droplet oscillation duration but also hinders bonding between droplets. As a result, the subsequent droplet quickly slides off the surface of the previous one and falls onto the substrate. To ensure optimal formation accuracy in metal droplet ejection printing, it is essential to minimize oxidation. Ideally, the deposition distance should be controlled to less than 4 mm.

The visual presentation of the aluminum droplet pile-up process at different oxidation levels is shown in Supplementary Video 3.

3.2.4. Effect of substrate feed speed on droplet oxidation morphology

Apart from the deposition distance, the substrate feed rate also plays a crucial role in droplet oxidation. During practical printing, the nozzle is not always positioned directly above the droplet to maintain continuous shielding gas coverage. Instead, the substrate moves dynamically along a path determined by the slicing data. The horizontal feed speed of the substrate dictates the duration of shielding gas protection, which directly impacts droplet oxidation behavior. The analysis above indicates a spatial correlation between wrinkle formation and oxidation. Wrinkle-rich regions on the droplet surface generally correspond to severe oxidized areas. Concurrently, previous studies (e.g., Nayebi & Divandari [65]; Jiang [70]) have shown that increased surface roughness and wrinkling are often associated with alumina film growth and instability. To facilitate the quantification of the droplet's oxidation level, a wrinkle index R was introduced. It is defined as the ratio of the wrinkle region height (h_o) to the total droplet height (h_d), expressed as $R{=}h_o/h_d$. The wrinkle index R is not a direct chemical measurement of oxidation, but rather a morphology-based metric that provides an intuitive indication of surface wrinkle distribution. The value of h_o was obtained from the droplet height profile using ImageJ, where the boundary between the wrinkled and smooth regions was identified by the inflection point of the grayscale gradient intensity.

In the experiment, the deposition distance H was set to 3.8 mm and the printing step distance L to 1 mm. The substrate was moved horizontally at various feed speeds F, as illustrated in Fig. 12a. Fig. 12b displays a positive correlation between the wrinkle index and the substrate feed speed. Each data point is the average of 15 droplets per condition. When the feed speed is held at 2.5 mm/s, the oxidation level remains comparable to that observed with a stationary substrate. Fig. 12c further shows that at feed speeds below 2 mm/s, the droplet surface remains smooth with minimal wrinkles. However, as the feed speed increases, droplet oxidation becomes progressively more pronounced. This increase is caused by three factors: higher substrate heat input, extended droplet solidification times, and reduced shielding gas protection duration at high feed speeds.

In this study, when the feed speed is less than 2.5 mm/s, the shielding gas effectively protects the droplet for a duration exceeding 0.4–0.5 s. This suggests that the shielding gas nozzle has an approximate effective protective radius of 1–1.25 mm. Furthermore, the duration of shielding gas protection significantly surpasses the ejection and deposition period of a single droplet. H. Merrow et al. [7] have established a relationship regarding the solidification time of metal droplets:

$$t_{sol} \approx \frac{D_d{}^2 \rho_L C_L}{4k}\left(\frac{1}{Ste} + \beta\right) \tag{11}$$

where k is the thermal conductivity of the substrate or droplet, depending on the one with the lower value; β accounts for droplet overheat, defined as $\beta = (T_d - T_{sub})/(T_L - T_{sub})$; Ste is the Stefan number used to describe the heat transfer from the droplet to the substrate, defined as $Ste = C_L(T_d - T_{sub})/H_f$, where T_{sub} is the substrate temperature. Taking $D_d = 560\ \mu m$, $T_d = 1023K$, and $T_{sub} = 573K$, the droplet solidification time could be calculated to be ~4.7 ms. This value is close to the normal oscillation duration shown in Fig. 7, but much shorter than the shielding gas protection duration. Since that the total ejection and deposition period is approximately 8.5 ms, once the melting temperature is reached, the droplet must cool for an additional 491.5 ms to prevent further oxidation. According to Newton's law of cooling, during this 491.5 ms post-solidification cooling phase, the droplet could reduce its temperature to ~749 K through heat conduction with the substrate. In practical printing processes, an engineering margin of approximately 10~15 % should be reserved. Therefore, the droplet surface temperature should be controlled at around 660 K.

3.3. Oxidation inhibition strategy for droplet printing under shielding gas

The surface oxidation level of aluminum droplets is fundamentally governed by the balance between their cooling duration and the shielding gas protection duration. If the shielding gas does not cover the entire deposition and cooling processes, the droplet's top surface will become prone to oxidation. This oxidation leads to wrinkle formation on the droplet surface. During the aluminum droplet printing, heat accumulation in the deposition layers reduces the cooling rate of the upper layers' droplets. Previous studies [77] have demonstrated that as the deposition frequency increases, heat accumulation within the layers accelerates. This effect disrupts the droplets' ability to maintain their intended shape, eventually causing coalescence.

In this study, radiation and convection losses to the ambient environment are assumed negligible. Thus, the majority of the heat carried by the droplet is transferred to the substrate via thermal conduction. If the droplet printing speed remains constant, heat accumulation would cause the surface temperature to gradually rise with increasing build height. To maintain thermal balance, the printing speed must be adjusted layer by layer. This ensures that heat input and dissipation remain in equilibrium, thereby keeping T_{surf} constant. When the influence of the actual print path on heat conduction within the deposited layer is neglected, and the current print layer is considered as a whole. Under this simplification, thermal accumulation can be described using a one-dimensional heat conduction model. By calculating the relationship between heat input and heat output, the thermal behavior of the

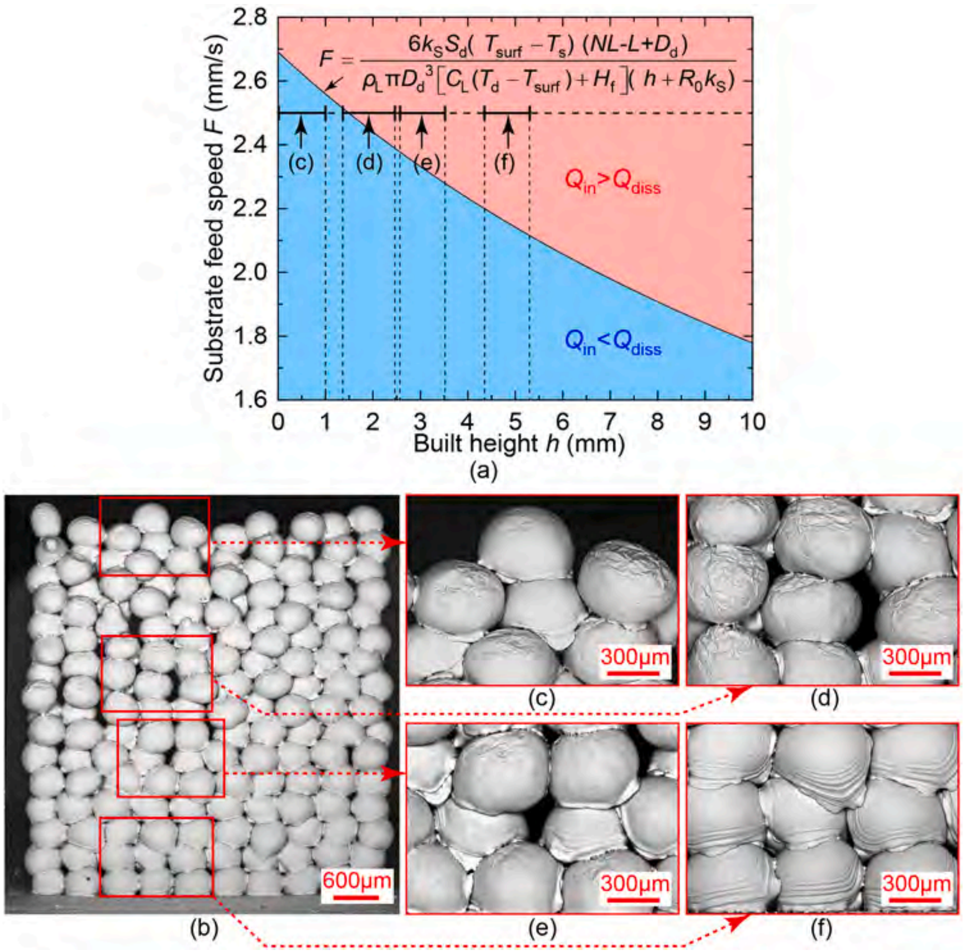

Fig. 13. (a) Relationship between the appropriate substrate feed speed and the built height. (b) SEM morphology of a thin-wall part deposited under a constant substrate feed speed. (c-f) are the droplet morphology of (b) at different built heights.

system can be semi-quantitatively described during the printing process. As the print layer cools from the initial temperature T_d to the steady surface temperature T_{surf}, the total heat input (Q_{in}) in the current printing layer can be approximated as [78]:

$$Q_{in} \approx \frac{N\rho_L \pi D_d^3}{6}\left[C_L\left(T_d - T_{surf}\right) + H_f\right], \tag{12}$$

where N is the droplet number of the current printing layer; T_{surf} is the surface temperature of the current printing layer. The energy released by each droplet is initially absorbed by a small region of the previously deposited layer or substrate. Over time, the accumulated energy is partially dissipated through vertical conduction to lower layers or the substrate. The total thermal resistance of the system is composed of the conduction resistance R_{cond} and the interfacial contact resistance $R_{contact}$, expressed as:

$$R_{total} = R_{cond} + R_{contact} = \frac{h}{k_S A_{base}} + \frac{R_0}{A_{base}}, \tag{13}$$

where h is the height of the previous built part; A_{base} is the effective heat conduction area, calculated as $A_{base} = NS_d$, here S_d is the effective conduction area per droplet; R_0 is the intrinsic contact resistance at the interface between the structure and the substrate, which could be evaluated as $\sim 10^{-4}$ (m^2·K)/W according to the previous study [79–82]. Therefore, the heat dissipation power of the system can be obtained as:

$$P_{diss} = \frac{T_{surf} - T_s}{\frac{h}{Nk_S S_d} + \frac{R_0}{NS_d}}, \tag{14}$$

To prevent thermal accumulation, the thermal input must be less than the dissipated heat for each layer printing cycle (Q_{diss}), that is:

$$Q_{in} < Q_{diss} = P_{diss}\Delta t. \tag{15}$$

Δt is the printing time of the current printing layer, which can be derived from the characteristic length of the current printing layer (l_0) and the substrate feed speed (F) as $\Delta t = l_0/F$. The characteristic length (l_0) can be estimated using $l_0 = L(N-1) + D_d$. Therefore, Eq. (15) can be further rewritten as:

$$Q_{in} < \frac{P_{diss}(LN - L + D_d)}{F}. \tag{16}$$

By combining Eqs. (12), (14), and (16), the relationship between the substrate feed speed F and the build height h can be obtained as:

$$F < \frac{6k_S S_d\left(T_{surf} - T_s\right)\left(NL - L + D_d\right)}{\rho_L \pi D_d^3\left[C_L\left(T_d - T_{surf}\right) + H_f\right]\left(h + R_0 k_S\right)}. \tag{17}$$

Based on the aforementioned analysis, it is essential to keep the substrate feed speed below 2.5 mm/s to ensure sufficient shielding gas protection duration. Consequently, the appropriate substrate feed speed (F_{safe}) should satisfy:

$$F_{safe}(h) < \min\left(\frac{6k_S S_d\left(T_{surf} - T_s\right)\left(NL - L + D_d\right)}{\rho_L \pi D_d^3\left[C_L\left(T_d - T_{surf}\right) + H_f\right]\left(h + R_0 k_S\right)}, 2.5 \times 10^{-3}\right). \tag{18}$$

To focus on the intrinsic thermal behavior of the system, the model is built under idealized assumption that droplets remain unoxidized

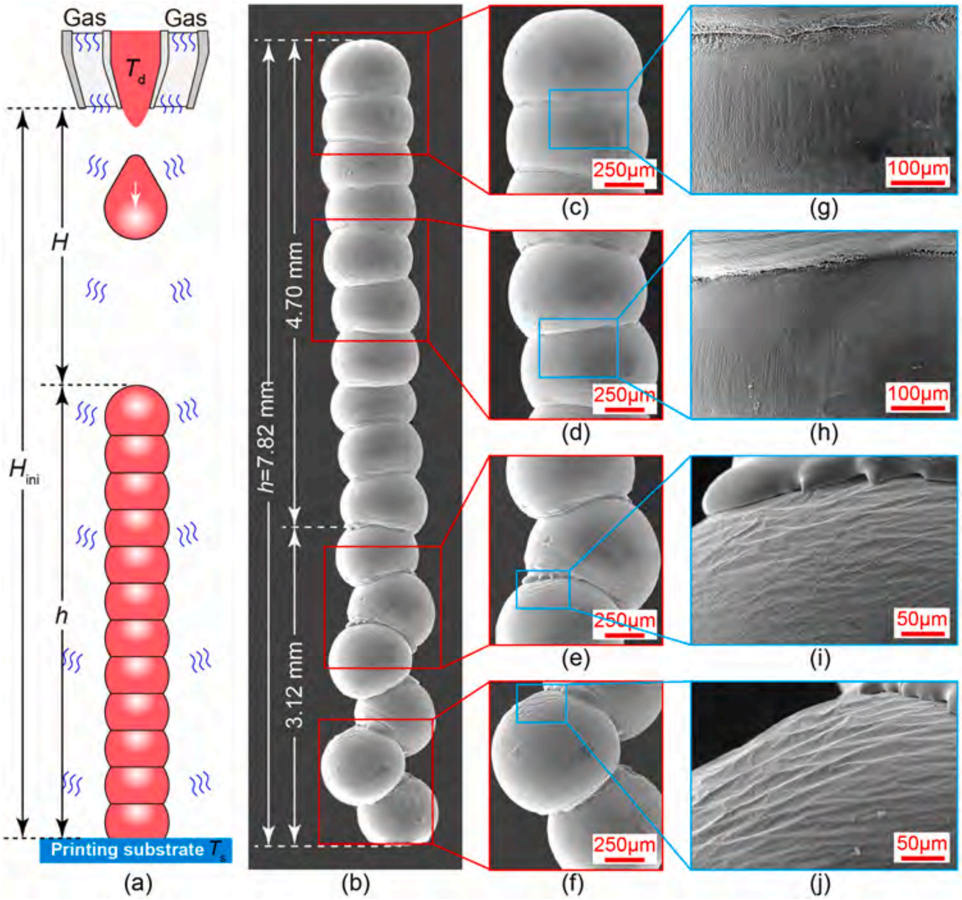

Fig. 14. (a) Schematic diagram of a one-dimensional column printing. (b) SEM morphology of the printed column. (c-j) Detail printing morphology of the column at different segments.

during deposition. Surface oxidation is known to increase surface roughness, elevate interfacial thermal resistance, and reduce wettability at the droplet interface. However, these effects are not explicitly included in the current model. The exclusion is due to two main reasons. First, consistent experimental data relevant to droplet oxidation are lacking. Second, oxidation strongly depends on oxide morphology, impurity distribution, and environmental conditions. This complexity makes direct modeling difficult. Future studies will aim to incorporate the influence of oxidation and its coupling with thermal transport and droplet dynamics.

Typical experimental conditions are $k_S = 195\text{W}\cdot\text{m}^{-1}\cdot\text{K}^{-1}$, $S \sim 10^{-7}\text{m}^2$, $\rho_L = 2415\text{kg}\cdot\text{m}^{-3}$, $D_d = 560$ µm,$C_L = 1050\text{J}\cdot\text{kg}^{-1}\cdot\text{K}^{-1}$, $T_d = 1023\text{K}$, $H_f = 3.97 \times 10^5\text{J/kg}$, $L = 550$ µm. Fig. 13a presents the dependence of the required substrate feed speed on the previously built height based on Eq. (17). As the built height increases from 0 mm to 10 mm, the required feed speed to prevent heat accumulation decreases from 2.7 mm/s to 1.8 mm/s. The critical substrate feed speed could be calculated from the built height as $F_{\text{safe}}(h) < \min(1/(19.06h + 0.37), 2.5)\text{mm/s}$.

Fig. 13b presents the SEM morphology of a thin-wall structure deposited with a printing step distance of 0.55 mm and a constant substrate feed speed of 2.5 mm/s. During printing, the substrate is continuously raised to maintain a constant droplet deposition distance of 3.8 mm. According to Eq. (18) and Fig. 13a, the maximum height for achieving unoxidized deposition under these parameters is 1.5 mm. Fig. 13c-f display the droplet morphology of the printed structure at various built heights. As depicted in Fig. 13f, the printed part exhibits good buildup morphology in the lower layers close to the substrate. However, as the built height increases, thermal accumulation prolongs solidification time, resulting in significant oxidation and noticeable wrinkle formation on the droplet surface (Fig. 13c,d). This oxidation negatively impacts the precision of material buildup, leading to increasingly irregular shaping as the built height grows in the thin-wall structure. This study focuses on qualitative trends through experimental characterization. Future work will incorporate computational fluid dynamics (CFD) simulations of shielding gas flow and transient oxidation kinetics. These simulations will be used to quantitatively predict local oxygen exposure and its correlation with oxidation behavior.

3.4. *Printing verification of aluminum droplets in an open environment*

A one-dimensional column printing experiment was conducted to validate the feasibility of this research. During the printing process, the melt temperature was kept at 1023 K, the substrate was heated to 573 K, and the shielding gas supply rate was set to 3.2 L/min. The distance between the substrate and the nozzle was kept constant at an initial deposition distance (H_{ini}) of 10 mm, as illustrated in Fig. 14a. To mitigate thermal accumulation, the droplet printing frequency was adjusted continuously according to $f(h) = F_{\text{safe}}(h) / D_d$ based on the built height. Fig. 14b presents the SEM morphology of the printed column, which had a total height of 7.82 mm. Near the column root, where the deposition distance is relatively large, lateral flight deviations and surface oxidation of droplets hinder high-precision printing. This results in an irregularly piled segment of 3.12 mm near the root, as seen in Fig. 14e,f. Oxidation wrinkles are also evident on the droplet surface (Fig. 14i,j). As the built height increases above 3.12 mm and the deposition distance falls below 6.88 mm, a uniform pile-up of 4.7 mm was obtained near the column tip. Concurrently, oxidation wrinkles on the droplet surface

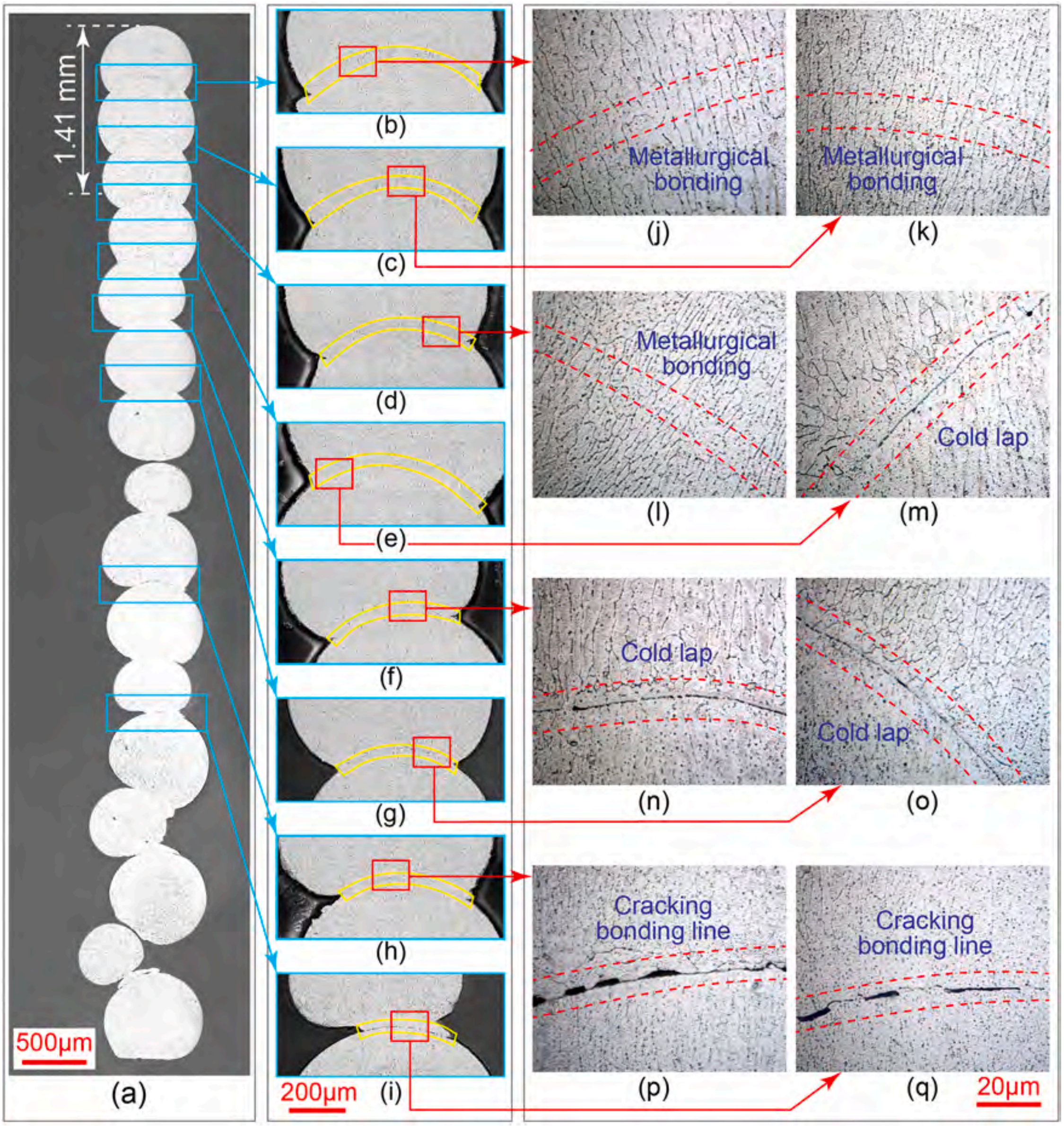

Fig. 15. (a) Internal cross-sectional morphology of the printed column. (b-i) Bonding morphology of the droplets at different built heights. (j-q) Corrosion grain morphology at the droplet bonding positions corresponding to (b-i).

gradually disappear, as shown in Fig. 14c,d,g,h. In addition, as the column height increases, the contact angle between adjacent droplets increases significantly. This is primarily attributed to variations in surface energy caused by oxidation. Changes in the geometrical morphology at the droplet top and the local temperature gradients may also contribute. During the column printing process, the reduction in droplet falling height and the rise in local temperature caused by heat accumulation can influence the surface tension and heat transfer of the droplets, thereby affecting their overall impact dynamics. However, parameters such as impact velocity and surface tension primarily determine the macroscopic solidification morphology rather than the microscopic wrinkle formation. The thermal accumulation effect may indirectly promote oxidation by extending the duration during which the droplet temperature remains above the critical level for oxide growth. Nevertheless, as shown in Fig. 14, the upper droplets, where heat accumulation is expected to be the most significant, did not exhibit noticeable wrinkling. In contrast, wrinkles appeared at the lower part of the column, where heat accumulation is minimal but oxygen exposure is relatively greater. This further indicates that the degree of wrinkling is more closely related to local oxygen exposure and shielding efficiency than to variations in impact dynamics or heat retention.

Longitudinal polishing and etching of the column shown in Fig. 14b revealed its internal cross-sectional morphology, as depicted in Fig. 15a. Fig. 15b-i display the bonding morphology of droplets at different heights within the column. Near the column root, irregular bonding morphologies are more prominent. Fig. 15j-q illustrate the etched grain structures at the droplet bonding interfaces corresponding to Fig. 15b-i. At a height of 1.41 mm near the column tip, where the droplet deposition distance is below 3.59 mm, no discernible grain separation lines are observed at the droplet bonding positions. This indicates strong metallurgical bonding, as shown in Fig. 15j-l. As the deposition distance increases, a relatively regular pile-up morphology could still be achieved. However, cold lap lines appear in the corresponding etched structures (Fig. 15m-o), which indicates weaker bonding quality. Closer to the bottom half of the column, oxidation-induced wrinkling and reduced wettability between droplets result in pronounced cracking along bonding lines, signifying poor bonding (Fig. 15p,q). The longer deposition distance at the bottom leads to insufficient gas shielding, resulting

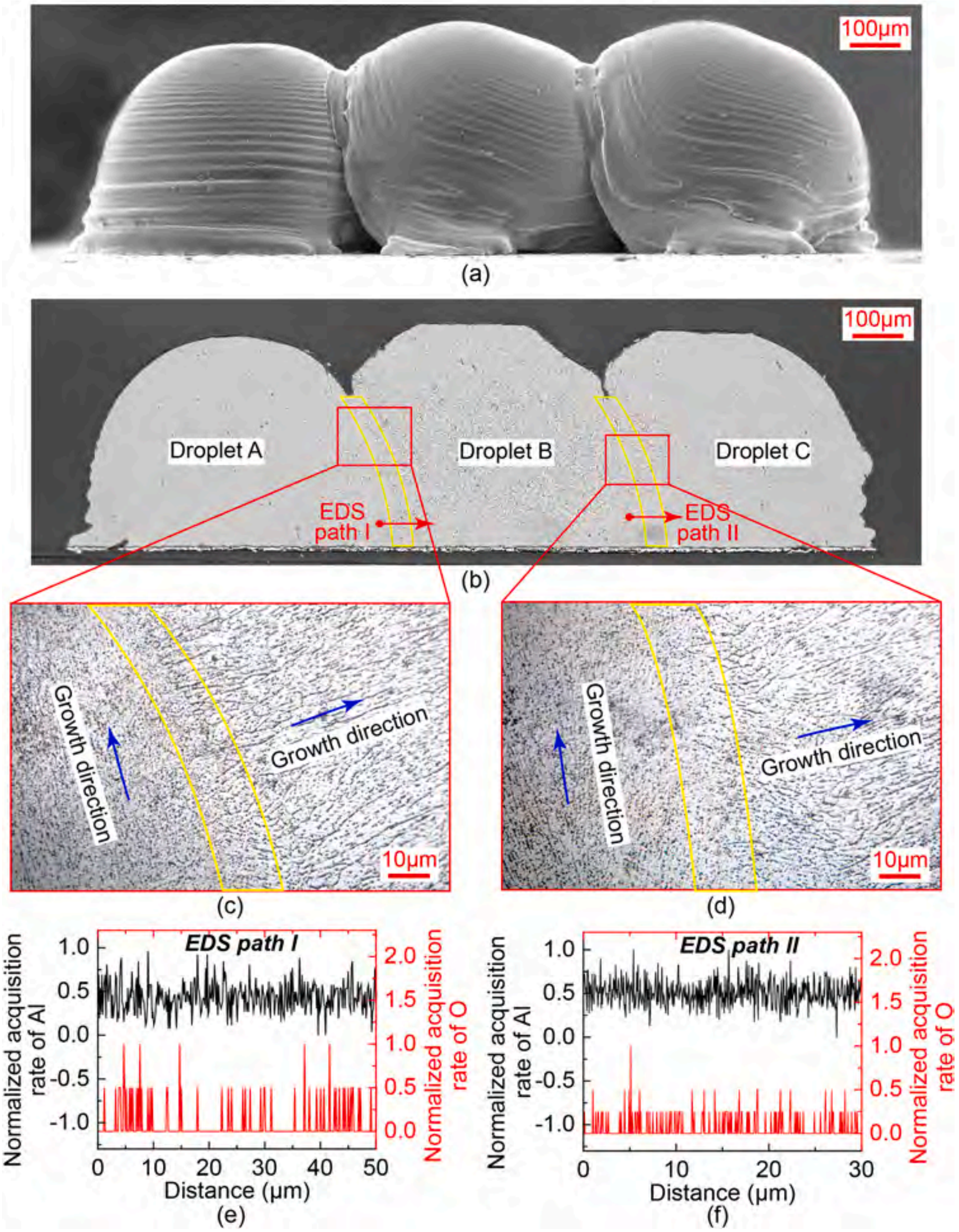

Fig. 16. (a) Overlapping morphology of three droplets. (b) Longitudinal cross-section of the polished droplet in (a). (c,d) Corrosion morphology of droplets at different bonding positions. (e,f) EDS line scan results of scanning paths I and II in (b), obtained before corrosion.

in severe oxidation that hinders wettability and causes bonding lines to crack, despite the presence of sufficient thermal energy for coalescence. Thus, maintaining a deposition distance within 3.59 mm is critical for oxidation suppression and reliable bonding.

An overlapping experiment involving three droplets was conducted by maintaining a droplet deposition distance of 3 mm and a printing step distance of 450 μm, as shown in Fig. 16a. The absence of oxidation wrinkles on the droplet surface indicates that surface oxidation was effectively suppressed under these conditions. To evaluate the bonding quality, the sample was longitudinally polished and etched, as illustrated in Fig. 16b. Fig. 16c,d display the etched grain morphology at different bonding locations. During the solidification of metal melts, dendritic structures grow preferentially along the heat flow direction. Thus, temperature gradients and solidification directions determine grain orientations at the droplet fusion interface during horizontal overlapping. At the interface, grains of the preceding droplet tend to grow vertically with the heat flow. In contrast, grains of the subsequent droplet, influenced by the temperature of the previously solidified droplet, tend to grow horizontally. Additionally, no visible defects, such as cold laps or cracking bonding lines, are observed at the droplet fusion interface from Fig. 16c,d. EDS line scan analysis was performed on the droplet cross-section before corrosion. Fig. 16e,f correspond to the scanning paths I and II in Fig. 16b, respectively. The results show that Al content stays consistently high, while O content remains low across bonding locations. No abrupt changes in element content were detected, confirming that strong metallurgical bonding of aluminum droplets under shielding gas protection is achieved.

To further assess the feasibility of forming structures in an open environment, aluminum alloy samples were printed using coaxial shielding gas. During printing, the melt temperature was kept at 1023 K, the substrate temperature at 573 K, and the shielding gas flow rate at 3.2 L/min. The deposition distance was set to 3 mm and the substrate feed speed was optimized according to the strategy detailed in Section 3.3. Fig. 17a shows a 10 × 10 aluminum alloy bump array printed in an

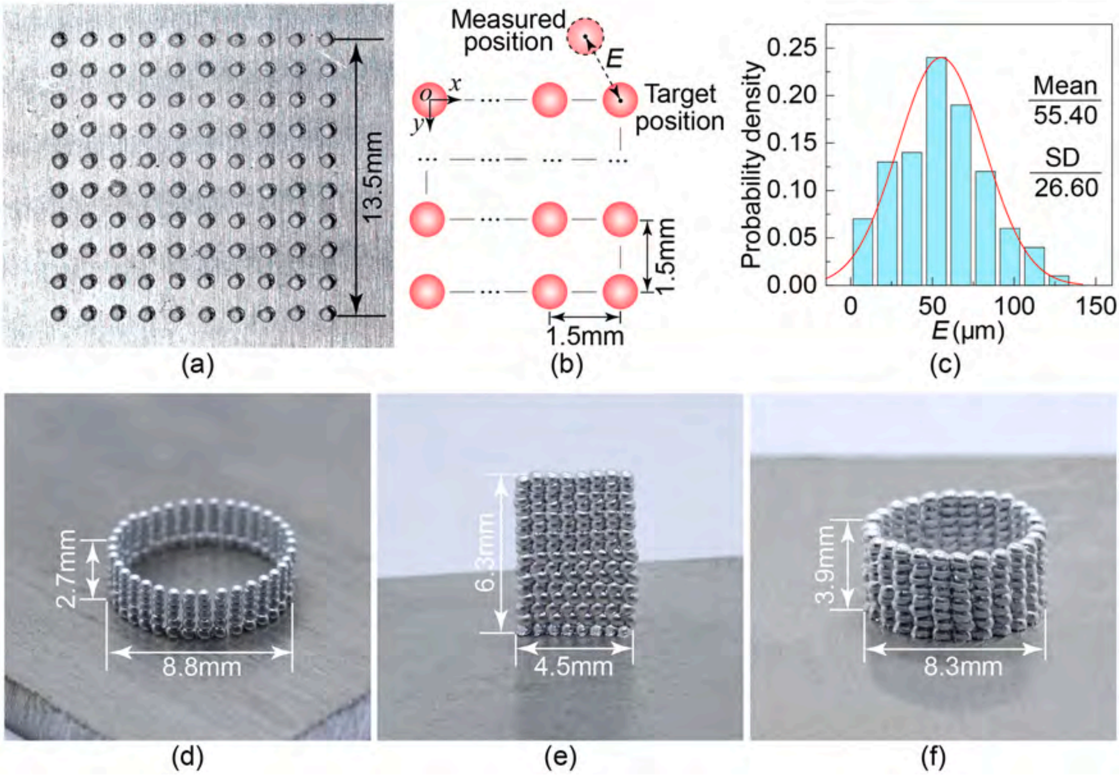

Fig. 17. Printing of aluminium alloy parts under coaxial shielding gas. (a) Printed 10 × 10 aluminium alloy bump array. (b) Schematic diagram of printing path for the aluminum alloy bump array. (c) Probability density of the droplet deposition errors. (d) Aluminium alloy column array. (e) Aluminium alloy thin-wall part. (f) Aluminium alloy cylindrical part.

open environment. The array was fabricated following a boustrophedon ("snake-like") path, as illustrated in Fig. 17b, with an inter-droplet spacing of 1.5 mm. The centroid coordinates of each bump were extracted using a grayscale centroid algorithm, and the droplet deposition positioning error (*E*) was calculated by comparing the measured positions with the target positions. Fig. 17c presents the statistically derived probability density of the droplet deposition errors. The positional errors follow an approximately normal distribution, with a mean error of 55.40 μm and a standard deviation of 26.60 μm. These correspond to 9.89 % and 4.75 % of droplet diameter, respectively. The results demonstrate that aluminum alloy droplets can achieve high accuracy printing even in an open environment. The visual presentation of the printing process for the 10 × 10 aluminum alloy bump array is provided in Supplementary Video 4. Fig. 17d-f present additional printed structures, including a column array, a thin-wall part, and a cylindrical part. These printed samples exhibit high precision and demonstrate the robust forming capability of aluminum droplets for open-environment deposition manufacturing.

4. Conclusions

In this work, a novel approach for open-environment printing of uniform aluminum droplets was demonstrated using piezoelectric actuation coupled with coaxial gas shielding. The key findings are as follows:

(1) Surface oxidation induces wrinkled morphologies on aluminum droplets. Increased deposition distance and substrate feed speed reduce the shielding effectiveness, suppressing droplet oscillation and intensifying surface wrinkling. Severe oxidation weakens droplet-substrate bonding, leading to rebound and decreased printing accuracy.

(2) A thermal management-based oxidation control strategy was proposed through droplet heat transfer analysis. In multi-layer printing, dynamically reducing the substrate feed speed prevents heat accumulation, effectively mitigating surface oxidation while promoting sound metallurgical bonding under coaxial gas shielding.

(3) The developed coaxial gas-shielded printing system enables high-precision fabrication of aluminum alloy components, validating the effectiveness of the open-environment deposition manufacturing technique for aluminum droplets.

Beyond the specific application to aluminum, the proposed thermal management strategy and oxidation control mechanism offer a generalized framework relevant to the additive manufacturing of other reactive metals in open environments. Future research will focus on unravelling the complex interactions between droplet dynamics and boundary conditions, such as droplet size, substrate topography, and material properties. Investigating these factors will provide deeper scientific insights into wetting behaviors and interfacial bonding mechanisms. These efforts, combined with the development of high-throughput deposition (>100 Hz), will further bridge the gap between laboratory research and industrial-scale manufacturing of high-performance metal components.

CRediT authorship contribution statement

Lehua Qi: Writing – review & editing, Supervision, Project administration, Methodology, Funding acquisition. **Lin Su:** Investigation. **Jun Luo:** Project administration, Funding acquisition. **Yi Zhou:** Writing – original draft, Validation, Software, Methodology, Investigation, Formal analysis, Data curation, Conceptualization.

Declaration of Competing Interest

The authors declare that they have no known competing financial interests or personal relationships that could have appeared to influence the work reported in this paper.

Acknowledgements

This work was supported by the National Natural Science Foundation of China (No. 52231004); the Natural Science Basic Research Program (Excellent Youth Foundation) of Shaanxi (No. 2024JC-JCQN-56); Shenzhen Science and Technology Program (JCYJ20210324121002006).

References

[1] Wright, K., Roberts, J., Stewart, C., 2020. The future of army supply chains and distribution-a possible model. Aust. Army J. 16, 79–100. ⟨https://search.informit.org/doi/10.3316/informit.333567470090748⟩.
[2] Kostidi, E., Nikitakos, N., Progoulakis, I., 2021. Additive manufacturing and maritime spare parts: Benefits and obstacles for the end-users. J. Mar. Sci. Eng. 9, 895. https://doi.org/10.3390/jmse9080895.
[3] Belhadi, A., Kamble, S.S., Venkatesh, M., Jabbour, C.J.C., Benkhati, I., 2022. Building supply chain resilience and efficiency through additive manufacturing: an ambidextrous perspective on the dynamic capability view. Int. J. Prod. Econ. 249, 108516. https://doi.org/10.1016/j.ijpe.2022.108516.
[4] Gupta, N., Tiwari, A., Bukkapatnam, S.T., Karri, R., 2020. Additive manufacturing cyber-physical system: supply chain cybersecurity and risks. IEEE Access 8, 47322–47333. https://doi.org/10.1109/ACCESS.2020.2978815.
[5] Ansell, T.Y., 2021. Current status of liquid metal printing. J. Manuf. Mater. Process 5, 31. https://doi.org/10.3390/jmmp5020031.
[6] Hu, G., Xue, B., Zhang, Y., Zhao, X., Wu, Y., He, W., Hao, F., Zhu, J., Li, Z., Li, D., 2025. Metal droplet ejection technology based on water hammer effect for additive manufacturing. J. Mater. Process. Technol. 338, 118785. https://doi.org/10.1016/j.jmatprotec.2025.118785.
[7] Merrow, H., Beroz, J.D., Zhang, K., Muecke, U.P., Hart, A.J., 2021. Digital metal printing by electrohydrodynamic ejection and in-flight melting of microparticles. Addit. Manuf. 37, 101703. https://doi.org/10.1016/j.addma.2020.101703.
[8] Qi, L.H., Chao, Y.P., Luo, J., Zhou, J.M., Hou, X.H., Li, H.J., 2012. A novel selection method of scanning step for fabricating metal components based on micro-droplet deposition manufacture. Int. J. Mach. Tools Manuf. 50–58. https://doi.org/10.1016/j.ijmachtools.2011.12.002.
[9] Yi, H., Li, J., Wang, Z., Cao, H., Liu, M., 2024. Elimination of gas entrapment in droplet-based 3D printing by induced electric-field. Int. J. Mech. Sci. 266, 108974. https://doi.org/10.1016/j.ijmecsci.2024.108974.
[10] Chao, Y.P., 2016. A novel selection method of slice thickness in metal micro-droplet deposition manufacture. J. Manuf. Process 21, 153–159. https://doi.org/10.1016/j.jmapro.2015.12.003.
[11] Li, S.L., Wei, Z.Y., Du, J., Zhao, G.X., Wang, X., Lu, B.H., 2016. Numerical and experimental investigation of molten metal droplet deposition applied to rapid prototyping. Appl. Phys. A Mater. Sci. Process 122, 1–5. https://doi.org/10.1007/s00339-016-0264-8.
[12] Lu, D., Xu, F.M., Zhao, L., Fu, Y.F., Dong, W., Tan, Y., Kawasaki, A., 2013. Fabrication of BGA solder balls by pulsated orifice ejection method. Piscataway, NJ. IEEE, pp. 694–697. https://doi.org/10.1109/ICEPT.2013.6756561.
[13] Ma, M., Wei, X.F., Shu, X.Y., Zhang, H.H., 2019. Producing solder droplets using piezoelectric membrane-piston-based jetting technology. J. Mater. Process. Technol. 263, 233–240. https://doi.org/10.1016/j.jmatprotec.2018.08.029.
[14] Meda, M., Mehta, P., Mahajan, C., Kahn, B., Cormier, D., 2021. Magnetohydrodynamic liquid metal droplet jetting of highly conductive electronic traces. Flex. Print. Electron 6, 035002. https://doi.org/10.1088/2058-8585/ac0fee.
[15] Zhang, C.J., Yang, Q., Yong, J.L., Shan, C., Zhang, J.Z., Hou, X., Chen, F., 2021. Guiding magnetic liquid metal for flexible circuit. Int. J. Extrem. Manuf. 3, 025102. https://doi.org/10.1088/2631-7990/abeda3.
[16] Luo, G., Wu, D., Zhou, Y., Hu, Y., Yao, Z., 2022. Laser printing of large-scale metal micro/nanoparticle array: Deposition behavior and microstructure. Int. J. Mach. Tools Manuf. 173, 103845. https://doi.org/10.1016/j.ijmachtools.2021.103845.
[17] Govekar, E., Jeromen, A., Kuznetsov, A., Kotar, M., Kondo, M., 2018. Annular laser beam based direct metal deposition. Procedia CIRP 74, 222–227. https://doi.org/10.1016/j.procir.2018.08.099.
[18] Bitharas, I., McPherson, N., McGhie, W., Roy, D., Moore, A.J., 2018. Visualisation and optimisation of shielding gas coverage during gas metal arc welding. J. Mater. Process. Technol. 255, 451–462. https://doi.org/10.1016/j.jmatprotec.2017.11.048.
[19] Rumschoettel, D., Griebel, B., Irlinger, F., Lueth, T.C., 2017. A fast pneumatic droplet generator for the ejection of molten aluminum. 2017 Pan Pacific Microelectronics Symposium. Pan Pacific, pp. 1–8. ⟨https://ieeexplore.ieee.org/abstract/document/7859574⟩.
[20] Himmel, B., 2020. Material Jetting of Aluminium: Analysis of a Novel Additive Manufacturing Process. PhD Diss. Technische Universität München, pp. 1–125.
[21] Rifat, U.A., 2023. Additive Manufacturing of 4008 Aluminum Via Magnetohydrodynamic Droplet Jetting. M. S. Degree Thesis Rochester Inst. Technol. 1–72.
[22] Sukhotskiy, V., Tawil, K., Einarsson, E., 2021. Printability regimes of pure metals using contactless magnetohydrodynamic drop-on-demand actuation. Phys. Fluids 33, 053303. https://doi.org/10.1063/5.0050354.
[23] Karampelas, I., Vader, S., Vader, Z., Sukhotskiy, V., Verma, A., Garg, G., Tong, M., Furlani, E., 2017. Drop-on-demand 3D metal printing. TechConnect Briefs 4, 213–215. https://doi.org/10.26153/tsw/16905.
[24] Fang, M., Chandra, S., Park, C.B., 2008. Building three-dimensional objects by deposition of molten metal droplets. Rapid Prototyp. J. 14, 44–52. https://doi.org/10.1108/13552540810841553.
[25] Amirzadeh, A., Raessi, M., Chandra, S., 2013. Producing molten metal droplets smaller than the nozzle diameter using a pneumatic drop-on-demand generator. Exp. Therm. Fluid. Sci. 47, 26–33. https://doi.org/10.1016/j.expthermflusci.2012.12.006.
[26] Yokoyama, Y., Endo, K., Iwasaki, T., Fukumoto, H., 2009. Variable-size solder droplets by a molten-solder ejection method. J. Micro Syst. 18, 316–321. https://doi.org/10.1109/JMEMS.2008.2011154.
[27] Yokoyama, Y., Fukumoto, H., Endo, K., Fujii, Y., Iwasaki, T., 2007. One picoliter ejection of solder droplets by an advanced molten solder ejection method. Mems. IEEE 20th Int. Conf. Kobe Jpn. 321–324. https://doi.org/10.1109/MEMSYS.2007.4433063.
[28] Tropmann, A., Lass, N., Paust, N., Metz, T., Ziegler, C., Zengerle, R., Koltay, P., 2011. Pneumatic dispensing of nano- to picoliter droplets of liquid metal with the StarJet method for rapid prototyping of metal microstructures. Microfluid. Nanofluid 12, 75–84. https://doi.org/10.1007/s10404-011-0850-1.
[29] Tropmann, A., Lass, N., Paust, N., Ziegler, C., Zengerle, R., Koltay, P., 2011. Monodisperse microparticle generation from aqueous solutions. SolidState Sens. Actuators Microsyst. Conf. Beijing China 1460–1463. https://doi.org/10.1109/TRANSDUCERS.2011.5969626.
[30] Zhou, Y., Qi, L., Lian, H., Luo, J., Su, L., 2024. Effect of impinging behavior annular jet shielding gas and printing substrate on metal droplet stable ejection. Addit. Manuf. 84, 104088. https://doi.org/10.1016/j.addma.2024.104088.
[31] Zhou, Y., Luo, J., Su, L., Qi, L., 2025. Suppression strategy for metal droplet overlapping fusion defects caused by droplet impact dynamics under coaxial shielding gas. Int. J. Heat. Mass Transf. 238, 126488. https://doi.org/10.1016/j.ijheatmasstransfer.2024.126488.
[32] Gerdes, B., Zengerle, R., Koltay, P., Riegger, L., 2018. Direct printing of miniscule aluminum alloy droplets and 3D structures by StarJet technology. J. Micromech. Micro 28, 074003. https://doi.org/10.1088/1361-6439/aab928.
[33] Traxel, K.D., Wilson-Heid, A.E., N. Watkins, N., M. Silva, C., Jeffries, J.R., J. Pascall, A., 2024. Microstructure and tensile properties of droplet-on-demand additively manufactured AlSi7Mg. Addit. Manuf. 87, 104215. https://doi.org/10.1016/j.addma.2024.104215.
[34] S. Vader, Z. Vader, Conductive liquid three dimensional printer, U.S. Patent US9616494B2. Apr. 11 2017.
[35] Wu, G., Wang, J., Tang, X., Gu, M., Chen, L., Shen, J., 2000. Isothermal oxidation of tin films. Acta Phys. Sin. Ch. Ed. 49, 1014–1018. https://doi.org/10.7498/aps.49.1014.
[36] Bonner, S.J., 2015. A microstructural and kinetic study of molten aluminium oxidation in relation to dross formation. PhD Diss. Univ. Qld. 138–145.
[37] Patouillet, K., Davoust, L., Doche, O., Delacroix, J., 2019. Mannheimer and Schechter model revisited: Viscosimetry of a (non-) Newtonian and curved interface. Phys. Rev. Fluids 4, 054002. https://doi.org/10.1103/PhysRevFluids.4.054002.
[38] Patouillet, K., Davoust, L., 2020. Between no slip and free slip: A new boundary condition for the surface hydrodynamics of a molten metal. Chem. Eng. Sci. 231, 116328. https://doi.org/10.1016/j.ces.2020.116328.
[39] Patouillet, K., Davoust, L., Doche, O., 2020. Viscosimetry of a non-Newtonian interface: The interesting role of MHD. Magnetohydrodynamics 56, 177–185. https://doi.org/10.22364/mhd.56.2-3.9.
[40] Shen, P., Fujii, H., Matsumoto, T., Nogi, K., 2004. Critical factors affecting the wettability of α-alumina by molten aluminum. J. Am. Ceram. Soc. 87, 2151–2159. https://doi.org/10.1111/j.1151-2916.2004.tb06376.x.
[41] Yang, W., Yang, R., Yao, Y., Gao, Z., Zhang, H., 2023. Effects of surface oxide layer on the impact dynamic behavior of molten aluminum droplets. Phys. Fluids 35, 013109. https://doi.org/10.1063/5.0136117.
[42] Yan, M., Fan, Z., 2001. Review durability of materials in molten aluminum alloys. J. Mater. Sci. 36, 285–295. https://doi.org/10.1023/A:1004843621542.
[43] Durst, F., Ray, S., Ünsal, B., Bayoumi, O., 2005. The development lengths of laminar pipe and channel flows. J. Fluid. Eng. T. ASME 1154–1160. https://doi.org/10.1115/1.2063088.
[44] Ai, Y., Zhang, Y., Han, S., Yan, Y., 2024. The analysis of microstructure evolution process considering the dynamic solidification conditions and flow field in the oscillating laser welding of aluminum alloy. Int. Commun. Heat. Mass 159, 107939. https://doi.org/10.1016/j.icheatmasstransfer.2024.107939.
[45] Chen, L., Mi, G., Zhang, X., Wang, C., 2021. Effects of sinusoidal oscillating laser beam on weld formation, melt flow and grain structure during aluminum alloys lap welding. J. Mater. Process. Technol. 298, 117314. https://doi.org/10.1016/j.jmatprotec.2021.117314.
[46] Li, Y., Zhao, Y., Zhou, X., Zhan, X., 2021. Effect of droplet transition on the dynamic behavior of the keyhole during 6061 aluminum alloy laser-MIG hybrid welding. Int. J. Adv. Manuf. Tech. 119, 897–909. https://doi.org/10.1007/s00170-021-08270-1.

[47] Chen, Y., Shao, Y., Xiao, X., 2023. A new method for predicting the morphology and surface roughness of micro grooves in aluminum alloy ablated by pulsed laser. J. Manuf. Process 96, 193–203. https://doi.org/10.1016/j.jmapro.2023.03.057.

[48] Schindelin, J., Rueden, C.T., Hiner, M.C., Eliceiri, K.W., 2015. The ImageJ ecosystem: An open platform for biomedical image analysis. Mol. Reprod. Dev. 82, 518–529. https://doi.org/10.1002/mrd.22489.

[49] Xu, Q., Oudalov, N., Guo, Q., Jaeger, H.M., Brown, E., 2012. Effect of oxidation on the Mechanical Properties of Liquid Gallium and Eutectic Gallium-Indium. Phys. Fluids 24, 299–606. https://doi.org/10.1063/1.4724313.

[50] Zhou, Y., Qi, L.H., Luo, J., Lin, S., 2023. Investigation on the Effect Mechanism of Micro-domain Shielding Gas on Metal Droplet Ejection Process (In Chinese). J. Mech. Eng. 59, 219–230. https://doi.org/10.3901/JME.2023.01.219.

[51] Aziz, S.D., Chandra, S., 2000. Impact, recoil and splashing of molten metal droplets. Int. J. Heat. Mass Transf. 43, 2841–2857. https://doi.org/10.1016/S0017-9310(99)00350-6.

[52] Pasandideh-Fard, M., Bhola, R., Chandra, S., Mostaghimi, J., 1998. Deposition of tin droplets on a steel plate: simulations and experiments. Int. J. Heat. Mass Transf. 41, 2929–2945. https://doi.org/10.1016/S0017-9310(98)00023-4.

[53] Pillai, S.K., Ando, T., 2009. Modeling of the in-flight solidification of droplets produced by the uniform-droplet spray process. Int. J. Therm. Sci. 48, 1494–1500. https://doi.org/10.1016/j.ijthermalsci.2008.12.011.

[54] Inoue, A., Masumoto, T., Ekimoto, T., Furukawa, S., Kuroda, Y., Chen, H.S., 1988. Preparation of Fe-, Co-, and Ni-Based amorphous alloy powders by high-pressure gas atomization and their structural relaxation behavior. Metall. Trans. A 19, 235–242. https://doi.org/10.1007/BF02652531.

[55] Luo, J., Qi, L.H., Zhong, S.Y., Zhou, J.M., Li, H.J., 2012. Printing solder droplets for micro devices packages using pneumatic drop-on-demand (DOD) technique. J. Mater. Process. Technol. 212, 2066–2073. https://doi.org/10.1016/j.jmatprotec.2012.05.007.

[56] Liu, H., Rangel, R.H., Lavernie, E.J., 1995. Modeling of droplet-gas interactions in spray atomization of Ta-2.5 W alloy. Mat. Sci. Eng. A 191, 171–184. https://doi.org/10.1016/0921-5093(94)09631-6.

[57] Dou, Y., Luo, J., Qi, L., Su, L., Lian, H., Huang, J., 2022. Quantitatively characterizing the evolution of hole defects between overlapped aluminum droplets by a two-dimensional solidification model. Addit. Manuf. 60, 103202. https://doi.org/10.1016/j.addma.2022.103202.

[58] Yi, H., Qi, L.H., Luo, J., Guo, Y., Li, S., Li, N., 2018. Elimination of droplet rebound off soluble substrate in metal droplet deposition. Mater. Lett. 216, 232–235. https://doi.org/10.1016/j.matlet.2018.01.127.

[59] Dowling, D.R., Dimotakis, P.E., 1990. Similarity of the concentration field of gas-phase turbulent jets. J. Fluid Mech. 218, 109–141. https://doi.org/10.1017/S0022112090000945.

[60] Larsson, I.S., Lycksam, H., Lundström, T.S., Marjavaara, B.D., 2020. Experimental study of confined coaxial jets in a non-axisymmetric co-flow. Exp. Fluids 61, 256. https://doi.org/10.1007/s00348-020-03094-3.

[61] Akselvoll, K., Moin, P., 1996. Large-eddy simulation of turbulent confined coannular jets. J. Fluid Mech. 315, 387–411. https://doi.org/10.1017/S0022112096002479.

[62] Stefanidou, M.K., Bloutsos, A.A., Dimas, A.A., Yannopoulos, P.C., 2025. Large Eddy simulation of annular plumes. Environ. Fluid Mech. 25, 29. https://doi.org/10.1007/s10652-025-10041-5.

[63] Gilani, N., Aboulkhair, N.T., Simonelli, M., East, M., Ashcroft, I.A., Hague, R.J.M., 2022. From impact to solidification in drop-on-demand metal additive manufacturing using MetalJet. Addit. Manuf. 55, 102827. https://doi.org/10.1016/j.addma.2022.102827.

[64] Cherng, J.-P.J., 1997. Solidification and cooling analysis of aluminum alloy droplets with the uniform droplet spray process. PhD Diss. MIT 33–47.

[65] Nayebi, B., Divandari, M., 2013. Characteristics of dynamically formed oxide films on molten aluminium. Int. J. Cast. Metal. Res. 25, 270–276. https://doi.org/10.1179/1743133612Y.0000000026.

[66] Xu, C., Gao, W., 2000. Pilling-Bedworth ratio for oxidation of alloys. Mater. Res. Innov. 3, 231–235. https://doi.org/10.1007/s100190050008.

[67] Montanini, R., Freni, F., 2012. A new method for the determination of the coefficient of thermal expansion of solid materials, 11th. Int. Conf. Quant. InfraRed Thermogr. Naples Italy 11–14. https://doi.org/10.21611/qirt.2012.175.

[68] Ali, R., Zafar, M., Manzoor, T., Kim, W.Y., Rashid, M.U., Abbas, S.Z., Zai, B.A., Ali, M., 2022. Elimination of solidification shrinkage defects in the casting of aluminum alloy. J. Mech. Sci. Technol. 36, 2345–2353. https://doi.org/10.1007/s12206-022-0416-z.

[69] Al-Sanabani, F.A., Madfa, A.A., Al-Qudaimi, N.H., 2014. Alumina ceramic for dental applications: A review article. Am. J. Mater. Res. 1, 26–34. ⟨https://www.researchgate.net/publication/261426535⟩.

[70] Jiang, B., 2025. The Effect of Oxidation Time on the Organization and Corrosion Performance of 6061 Aluminum Alloy Micro-Arc Oxidation Coatings. Coatings 15, 1–15. https://doi.org/10.3390/coatings15020117.

[71] T. Jonsson, On the one dimensional Stefan problem: with some numerical analysis, B.S. Degree Thesis. Umeå University (2013) 8-16.

[72] Hart, R., Maurin, J., 1970. The nucleation and growth of oxide islands on aluminum. Surf. Sci. 20, 285–303. https://doi.org/10.1016/0039-6028(70)90182-2.

[73] Salas, O., Ni, H., Jayaram, V., Vlach, K., Levi, C., Mehrabian, R., 1991. Nucleation and growth of Al2O3/metal composites by oxidation of aluminum alloys. J. Mater. Res. 6, 1964–1981. https://doi.org/10.1557/JMR.1991.1964.

[74] Jeurgens, L., Sloof, W., Tichelaar, F., Mittemeijer, E., 2002. Growth kinetics and mechanisms of aluminum-oxide films formed by thermal oxidation of aluminum. J. Appl. Phys. 92, 1649–1656. https://doi.org/10.1063/1.1491591.

[75] Nguyen, L., Hashimoto, T., Zakharov, D.N., Stach, E.A., Rooney, A.P., Berkels, B., Thompson, G.E., Haigh, S.J., Burnett, T.L., 2018. Atomic-scale insights into the oxidation of aluminum. ACS Appl. Mater. Interfaces 10, 2230–2235. ⟨https://pubs.acs.org/doi/10.1021/acsami.7b17224⟩.

[76] Bergsmark, E., Simensen, C., Kofstad, P., 1989. The oxidation of molten aluminum. Mater. Sci. Eng. A 120, 91–95. https://doi.org/10.1016/0921-5093(89)90723-5.

[77] Liu, M., Yi, H., Cao, H., Huang, R., Jia, L., 2021. Heat accumulation effect in metal droplet-based 3D printing: Evolution mechanism and elimination Strategy. Addit. Manuf. 48, 102413. https://doi.org/10.1016/j.addma.2021.102413.

[78] Fang, M., Chandra, S., Park, C.B., 2007. Experiments on Remelting and Solidification of Molten Metal Droplets Deposited in Vertical Columns. J. Manuf. Sci. E. 129, 461–466. https://doi.org/10.1115/1.2540630.

[79] Loulou, T., Artyukhin, E., Bardon, J., 1999. Estimation of thermal contact resistance during the first stages of metal solidification process: I—experiment principle and modelisation. Int. J. Heat. Mass Tran 42, 2119–2127. https://doi.org/10.1016/S0017-9310(98)00333-0.

[80] Loulou, T., Artyukhin, E., Bardon, J., 1999. Estimation of thermal contract resistance during the first stages of metal solidification process: II—experimental setup and results. Int. J. Heat. Mass Tran 42, 2129–2142. https://doi.org/10.1016/S0017-9310(98)00338-X.

[81] Gilani, N., Aboulkhair, N.T., Simonelli, M., East, M., Ashcroft, I., Hague, R.J.M., 2021. Insights into drop-on-demand metal additive manufacturing through an integrated experimental and computational study. Addit. Manuf. 48, 102402. https://doi.org/10.1016/j.addma.2021.102402.

[82] Minakov, A., Morikawa, J., Ryu, M., Zhuravlev, E., Schick, C., 2022. Interfacial thermal conductance of 7075 aluminum alloy microdroplets in contact with a solid at fast melting and crystallization. Mater. Res. Express 9, 086503. https://doi.org/10.1088/2053-1591/ac859b.

Yi Zhou is currently a Ph.D. student at School of Mechanical Engineering, Northwestern Polytechnical University. His research interests include dynamic behaviors of metal droplet ejection and impacting, electronics packaging technology, and the construction technology of micro-domain shielding gas for metal droplet-based 3D printing.

Jun Luo is a Full Professor at Research and Development Institute of Northwestern Polytechnical University in Shenzhen, School of Mechanical Engineering, Northwestern Polytechnical University. His research mainly lies in electronics packaging technology, metal jet breakup simulation, droplet charging and deflection, and laser-induced micro-droplet 3D printing.

Lin Su is currently a Ph.D. student at School of Mechanical Engineering, Northwestern Polytechnical University. His research focuses on additive manufacturing technology based on magnesium droplet ejection, heat and mass transfer of magnesium droplet printing.

Lehua Qi (Corresponding author) is a Full Professor at Research and Development Institute of Northwestern Polytechnical University in Shenzhen, School of Mechanical Engineering, Northwestern Polytechnical University. Her research interests include metal droplet-based 3D printing technology, semi-solid forming technology and application of metal matrix composites, and image recognition of C/C composites.